

1 **Atmospheric energy budget response to idealized aerosol perturbation in**
2 **tropical cloud systems**

3 **Guy Dagan¹, Philip Stier¹, Matthew Christensen¹, Guido Cioni^{2,3}, Daniel Klocke^{3,4} and Axel**
4 **Seifert⁴**

5 ¹ Atmospheric, Oceanic and Planetary Physics, Department of Physics, University of Oxford, UK

6 ² Max Planck Institute for Meteorology, Hamburg, Germany

7 ³ Hans Ertel Center for Weather Research, Offenbach am Main, Germany

8 ⁴ Deutscher Wetterdienst, Offenbach am Main, Germany

9 E-mail: guy.dagan@physics.ox.ac.uk

10
11 **Abstract**

12 The atmospheric energy budget is analysed in numerical simulations of tropical cloud systems
13 to better understand the physical processes behind aerosol effects on the atmospheric energy
14 budget. The simulations include both shallow convective clouds and deep convective tropical
15 clouds over the Atlantic Ocean. Two different sets of simulations, at different dates (10-
16 12/8/2016 and 16-18/8/2016), are simulated with different dominant cloud modes (shallow or
17 deep). For each case, the cloud droplet number concentrations (CDNC) is varied as a proxy for
18 changes in aerosol concentrations. It is shown that the total column atmospheric radiative cooling
19 is substantially reduced with CDNC in the deep-cloud dominated case (by $\sim 10.0 \text{ W/m}^2$), while a
20 much smaller reduction ($\sim 1.6 \text{ W/m}^2$) is shown in the shallow-cloud dominated case. This trend
21 is caused by an increase in the ice and water vapor content at the upper troposphere that leads to
22 a reduced outgoing longwave radiation, an effect which is stronger under deep-cloud dominated
23 conditions. A decrease in sensible heat flux (driven by increase in the near surface air
24 temperature) reduces the warming by $\sim 1.4 \text{ W/m}^2$ in both cases. It is also shown that the cloud
25 fraction response behaves in opposite ways to an increase in CDNC, showing an increase in the
26 deep-cloud dominated case and a decrease in the shallow-cloud dominated case. This
27 demonstrates that under different environmental conditions the response to aerosol perturbation
28 could be different.

30 Introduction

31 The negative anthropogenic radiative forcing due to aerosols is acting to cool the climate and to
32 compensate some of the warming due to increase in greenhouse gases (Boucher et al., 2013).
33 However, quantification of this effect is highly uncertain with a revised uncertainty range of
34 -1.60 to -0.65 W/m^2 (Bellouin et al., 2019). The total anthropogenic aerosol radiative forcing is
35 composed of contribution from direct interaction of aerosols with radiation (scattering and
36 absorption) and from indirect interaction with radiation due to changes in cloud properties.

37 Beside its effect on the radiation budget, aerosols may affect the precipitation distribution and
38 total amount (Levin and Cotton, 2009; Albrecht, 1989; Tao et al., 2012). A useful perspective to
39 improve our understanding of aerosol effect on precipitation, which became common in the last
40 few years, arises from constraints on the energy budget (O’Gorman et al., 2012; Muller and
41 O’Gorman, 2011; Hodnebrog et al., 2016; Samset et al., 2016; Myhre et al., 2017; Liu et al.,
42 2018; Richardson et al., 2018; Dagan et al., 2019a). On long time scales, any precipitation
43 perturbations by aerosol effects will have to be balanced by changes in radiation fluxes, sensible
44 heat flux or by divergence of dry static energy. The energy budget constraint perspective was
45 found useful to explain both global (e.g. (Richardson et al., 2018)) and regional (Liu et al., 2018;
46 Dagan et al., 2019a) precipitation response to aerosol perturbations in global scale simulations.
47 In this study, we investigate the energy budget response to aerosol perturbation on a regional
48 scale using high resolution cloud resolving simulations. This enables an improved understanding
49 of the microphysical processes controlling atmospheric energy budget perturbations. The strong
50 connection between the atmospheric energy budget and convection has long been appreciated
51 (e.g. (Arakawa and Schubert, 1974; Manabe and Strickler, 1964)) as well as the connection to
52 the general circulation of the atmosphere (Emanuel et al., 1994).

53 The total column atmospheric energy budget can be described as follows:

$$54 \quad LP + Q_R + Q_{SH} = \text{div}(s) + ds/dt \quad (1)$$

55 Equation 1 presents a balance between the latent heating rate (LP - latent heat of condensation
56 [L] times the surface precipitation rate [P]), the surface sensible heat flux (Q_{SH}), the atmospheric
57 radiative heating (Q_R), the divergence of dry static energy ($\text{div}(s)$, which will become negligible
58 on sufficiently large spatial scales), and the dry static energy storage term (ds/dt , which will
59 become negligible on long [inter-annual] temporal scales). Throughout the rest of this paper we

60 will refer to the right-hand side of Equation 1 ($\text{div}(s)+ds/dt$) as the energy imbalance (which is
61 calculated as the residual [R] of the left-hand side).

62 Q_R is defined as:

$$63 \quad Q_R = (F_{SW}^{TOA} - F_{SW}^{SFC}) + (F_{LW}^{TOA} - F_{LW}^{SFC}) \quad (2)$$

64 and represents the rate of net atmospheric diabatic warming due to radiative shortwave (SW) and
65 longwave (LW) fluxes. It is expressed by the sum of the surface (SFC) and top of the atmosphere
66 (TOA) fluxes, when all fluxes are positive downwards. As in the case of TOA radiative forcing,
67 aerosols could modify the atmospheric energy budget by both direct interaction with radiation
68 and by microphysical effects on clouds. The latter is the focus of this study.

69 The microphysical effects are driven by the fact that aerosols serve as cloud condensation nuclei
70 (CCN) and ice nuclei (IN). Larger aerosol concentrations, e.g. by anthropogenic emissions, could
71 lead to larger cloud droplet and ice particle concentrations (Andreae et al., 2004; Twomey, 1977;
72 Hoose and Möhler, 2012). Changes in hydrometer concentration and size distribution were
73 shown to affect clouds' microphysical processes rates (such as condensation, evaporation,
74 freezing and collision-coalescence), which in turn could affect the dynamics of the clouds (Khain
75 et al., 2005; Koren et al., 2005; Heikenfeld et al., 2019; Chen et al., 2017; Altaratz et al., 2014;
76 Seifert and Beheng, 2006a), the rain production (Levin and Cotton, 2009; Albrecht, 1989; Tao
77 et al., 2012) and the clouds' radiative effect (Koren et al., 2010; Storelvmo et al., 2011; Twomey,
78 1977; Albrecht, 1989). The aerosol effect, and in particular its effects on the radiation budget
79 and the atmospheric energy budget, is cloud regime dependent (Altaratz et al., 2014; Lee et al.,
80 2009; Mülmenstädt and Feingold, 2018; van den Heever et al., 2011; Rosenfeld et al., 2013;
81 Glassmeier and Lohmann, 2016; Gryspeerdt and Stier, 2012; Christensen et al., 2016), time
82 dependent (Dagan et al., 2017; Gryspeerdt et al., 2015; Seifert et al., 2015; Lee et al., 2012;
83 Dagan et al., 2018c), aerosol type and size distribution dependent (Jiang et al., 2018; Lohmann
84 and Hoose, 2009) and (even for a given cloud regime) meteorological conditions dependent
85 (Dagan et al., 2015a; Fan et al., 2009; Fan et al., 2007; Kalina et al., 2014; Khain et al., 2008)
86 and was shown to be non-monotonic (Dagan et al., 2015b; Jeon et al., 2018; Gryspeerdt et al.,
87 2019; Liu et al., 2019). Hence the quantification of the global mean radiative effect is extremely
88 challenging (e.g. (Stevens and Feingold, 2009; Bellouin et al., 2019)).

89 Previous studies demonstrated that the mean aerosol effect on deep convective clouds can
90 increase the upward motion of water, and hence also increase the cloud anvil mass and extent

91 (Fan et al., 2010; Chen et al., 2017; Fan et al., 2013; Grabowski and Morrison, 2016). The
92 increase in mass flux to upper levels was explained by the convective invigoration hypothesis
93 (Fan et al., 2013; Koren et al., 2005; Rosenfeld et al., 2008; Seifert and Beheng, 2006a; Yuan
94 et al., 2011a; Williams et al., 2002), which was proposed to lead to stronger latent heat release
95 under higher aerosol concentrations and hence stronger vertical velocities. In addition to the
96 stronger vertical velocities, under polluted conditions the smaller hydrometers are being
97 transported higher in the atmosphere (for a given vertical velocity (Chen et al., 2017; Koren et
98 al., 2015; Dagan et al., 2018a)) and their lifetime at the upper troposphere is longer (Fan et al.,
99 2013; Grabowski and Morrison, 2016). The invigoration mechanism can also lead to an increase
100 in precipitation (Khain, 2009; Altaratz et al., 2014). Both the increase in precipitation and the
101 increase in anvil coverage would act to warm the atmospheric column: the increased precipitation
102 by latent heat release, and the increased anvil mass and extent by longwave radiative warming
103 (Koren et al., 2010; Storelvmo et al., 2011). However, it should be pointed out that the
104 uncertainty underlying these proposed effects remain significant (White et al., 2017; Varble,
105 2018). In addition, aerosol effects on precipitation from deep convective cloud was shown to be
106 non-monotonic and depend on the aerosol range (Liu et al., 2019).

107 In the case of shallow clouds, aerosol effect on precipitation was also shown to be non-monotonic
108 (Dagan et al., 2015a; Dagan et al., 2017). However, unlike in the deep clouds case, the mean
109 effect on precipitation, under typical modern-day conditions, is thought to be negative (Albrecht,
110 1989; Rosenfeld, 2000; Jiang et al., 2006; Xue and Feingold, 2006; Dagan and Chemke, 2016).
111 The aerosol effect on shallow cloud cover and mean water mass (measure by liquid water path -
112 LWP) might also depend on the meteorological conditions and aerosol range (Dagan et al.,
113 2015b; Dagan et al., 2017; Gryspeerd et al., 2019; Dey et al., 2011; Savane et al., 2015) and is
114 the outcome of competition between different opposing response of: rain suppression (that could
115 lead to increase in cloud lifetime and coverage (Albrecht, 1989)), warm clouds invigoration (that
116 could also lead to increase in cloud coverage and LWP (Koren et al., 2014; Kaufman et al., 2005;
117 Yuan et al., 2011b)) and increase in entrainment and evaporation (that could lead to decrease in
118 cloud coverage (Small et al., 2009; Jiang et al., 2006; Costantino and Bréon, 2013; Seigel,
119 2014)). Another addition to this complex response is the fact that the aerosol effect on warm
120 convective clouds was shown to be time dependent and affected by the clouds' feedbacks on the
121 thermodynamic conditions (Seifert et al., 2015; Dagan et al., 2016; Dagan et al., 2017; Lee et al.,
122 2012; Stevens and Feingold, 2009; Dagan et al., 2018b). Previous simulations that contained
123 several tropical cloud modes demonstrate that increase in aerosol concentrations can lead to

124 suppression of the shallow mode and invigoration of the deep mode (van den Heever et al., 2011).
125 Hence the domain mean effect, even if it is demonstrated to be small, may be the result of
126 opposing relatively large contributions from the different cloud modes (van den Heever et al.,
127 2011). The small domain mean effect may suggest that on large enough scales the energy (Muller
128 and O’Gorman, 2011; Myhre et al., 2017) or water budget (Dagan et al., 2019b) constrain
129 precipitation changes.

130 Previous studies, using global simulations (O’Gorman et al., 2012; Muller and O’Gorman, 2011;
131 Hodnebrog et al., 2016; Samset et al., 2016; Myhre et al., 2017; Liu et al., 2018; Richardson et
132 al., 2018; Dagan et al., 2019a), demonstrated the usefulness of the atmospheric energy budget
133 perspective in constraining aerosol effect on precipitation. However, the physical processes
134 behind aerosol-cloud microphysical effects on the energy budget are still far from being fully
135 understood. In this study we use cloud resolving simulations to increase our understanding of the
136 effect of microphysical aerosol-cloud interactions on the atmospheric energy budget.

137 **Methodology**

138 The icosahedral nonhydrostatic (ICON) atmospheric model (Zängl et al., 2015) is used in a
139 limited area configuration. ICON’s non-hydrostatic dynamical core was evaluated with several
140 idealized cases (Zängl et al., 2015). The simulations are conducted such that they are aligned
141 with the NARVAL 2 (Next-generation Aircraft Remote-Sensing for Validation Studies (Klepp
142 et al., 2014; Stevens et al., 2019; Stevens et al., 2016)) campaign, which took place during August
143 2016 in the western part of the northern tropical Atlantic. We use existing NARVAL 2
144 convection-permitting simulations (Klocke et al., 2017) as initial and boundary conditions for
145 our simulations.

146 The domain covers $\sim 22^\circ$ in the zonal direction ($25^\circ - 47^\circ$ W) and $\sim 11^\circ$ in the meridional direction
147 ($6^\circ - 17^\circ$ N) and therefore a large fraction of the northern tropical Atlantic (Fig. 1). During August
148 2016, the intertropical convergence zone (ITCZ) was located in the southern part of the domain
149 while the northern part mostly contains trade cumulus clouds. Hence, this case study provides
150 an opportunity to study heterogenous clouds systems. Daily variations in the deep/shallow cloud
151 modes in our domain were observed, but it always included both cloud modes, albeit in different
152 relative fraction. Two different dates are chosen, one representing a shallow-cloud dominated
153 mode (10-12/8/2016 – see Fig. 2, and Figs S1 and S3, supporting information- SI), and one that
154 represents a deep-cloud dominated mode (16-18/8/16 – see Fig. 3 and Figs. S2 and S3, SI). In

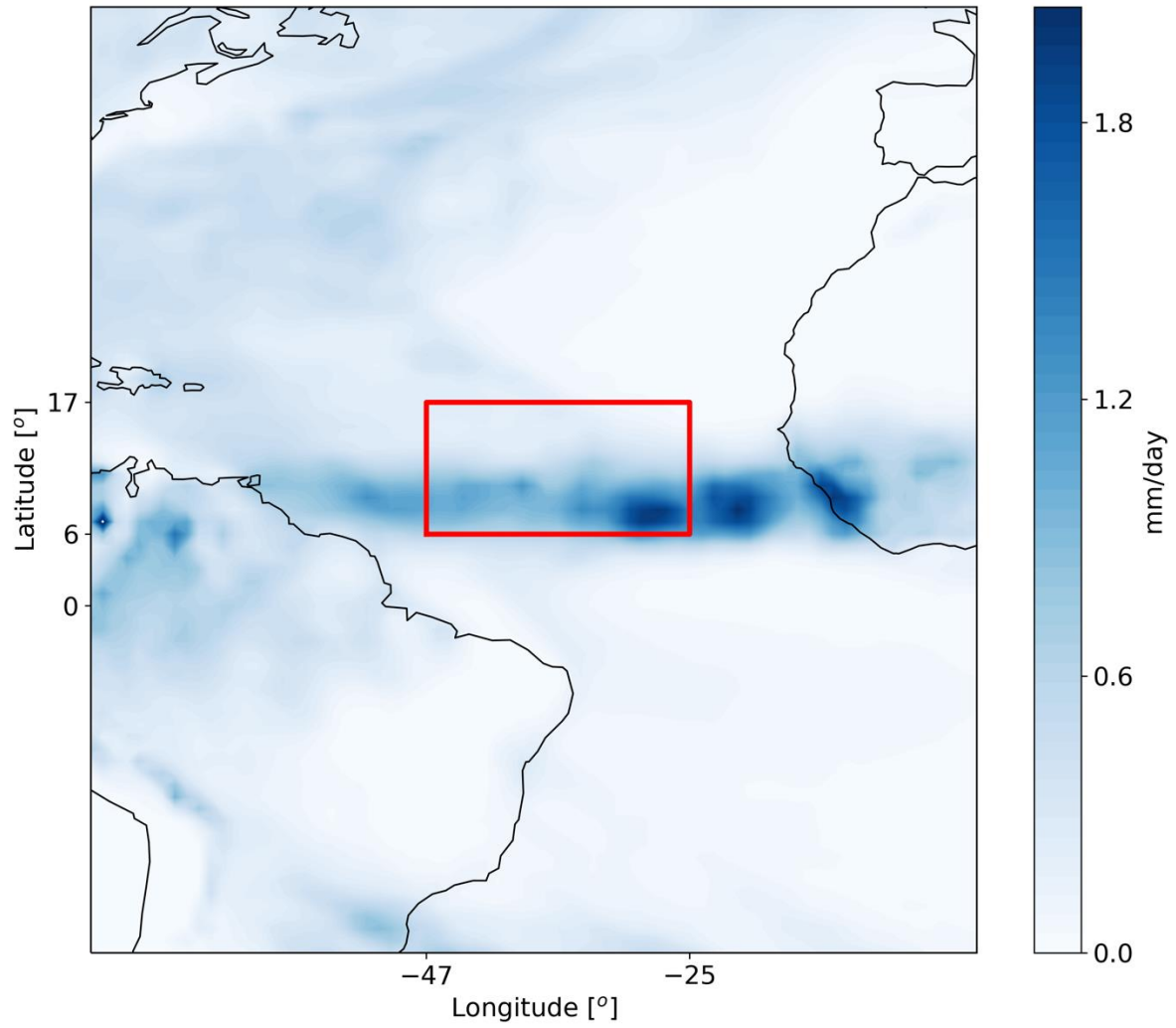
155 the shallow-cloud dominated case, most of the domain is covered by trade cumulus clouds that
156 are being advected with the trade winds from north-east to south-west. In the southern part of the
157 domain, throughout most of the simulation, there is a zonal band of deep convective clouds (Fig.
158 2) that contribute on average ~25% out of the total cloud cover (Fig. S3, SI). The deep-cloud
159 dominated case represents the early stages of the development of the tropical storm Fiona (Fig.
160 3). Fiona formed in the eastern tropical Atlantic and moved toward the west-north-west. It started
161 as a tropical depression at 16/8/2016 18:00 UTC while its centre was located at 12.0° N 32.2° W.
162 It kept moving towards the north-west and reach a level of a tropical storm at 17/8/2016 12UTC,
163 while its centre was located at 13.7° N 36.0° W
164 (https://www.nhc.noaa.gov/data/tcr/AL062016_Fiona.pdf). The general propagation speed and
165 direction, strength (measure by maximal surface wind speed) and location of the storm are
166 predicted well by the model. However, the model produces more anvil clouds than what was
167 observed from the satellite (Fig. 3). These two different cases, representing different atmospheric
168 energy budget initial state (see also Figs. 4 and 12 below), enable the investigation of the aerosol
169 effect on the energy budget under different initial conditions.

170 We use a two-moment bulk microphysical scheme (Seifert and Beheng, 2006b). For each case,
171 four different simulations with different prescribed cloud droplet number concentrations
172 (CDNC) of 20, 100, 200, and 500 cm⁻³ are conducted. The different CDNC scenarios serve as
173 a proxy for different aerosol conditions (as the first order effect of increased aerosol
174 concentration on clouds is to increase the CDNC, Andreae, 2009). This also allows to separate
175 the cloud response from the uncertainties involved in the representation of the aerosols in
176 numerical models (Ghan et al., 2011; Simpson et al., 2014; Rothenberg et al., 2018). However,
177 it limits potential feedbacks between clouds and aerosols, such as the removal of aerosol levels
178 by precipitation scavenging and potential aerosol effects thereon. In addition, the fixed CDNC
179 framework does not capture the differences in aerosol activation between shallow and deep
180 clouds, due to differences in vertical velocity. Another aerosol effect that is not included in our
181 simulations is the direct interaction between aerosol and radiation. In future work we plan to
182 examine the mutual interaction between the microphysical effects and the direct aerosol
183 radiative effects.

184 For calculation of the difference between high CDNC (polluted) conditions and low CDNC
185 (clean) conditions, the simulations with CDNC of 200 and 20 cm⁻³ are chosen as they represent
186 the range typically observed over the ocean (see for example the CDNC range presented in

187 recent observational-based studies (Rosenfeld et al., 2019; Gryspeerdt et al., 2019)). Each
188 simulation is conducted for 48 hours starting from 12 UTC. The horizontal resolution is set to
189 1200 m and 75 vertical levels are used. The temporal resolution is 12 sec and the output interval
190 is 30 min. Interactive radiation is calculated every 12 min using the RRTM-G scheme (Clough
191 et al., 2005; Iacono et al., 2008; Mlawer et al., 1997). We have added a coupling between the
192 microphysics and the radiation to include the Twomey effect (Twomey, 1977). This was done
193 by including the information of the cloud liquid droplet effective radius, calculated in the
194 microphysical scheme, in the radiation calculations. No Twomey effect due to changes in the
195 ice particles size distribution was considered due to the large uncertainty involved in the ice
196 microphysics and morphology. Additional details, such as the surface and atmospheric physics
197 parameterizations, are described in Klocke et al., (2017) and include an interactive surface flux
198 scheme and fixed sea surface temperature (SST). We note that using a fixed SST does not
199 include feedbacks of aerosols on the SST evolution that could change the surface fluxes.
200 However, due to the large heat capacity of the ocean, we do not expect the SST to dramatically
201 change over the two days simulations.

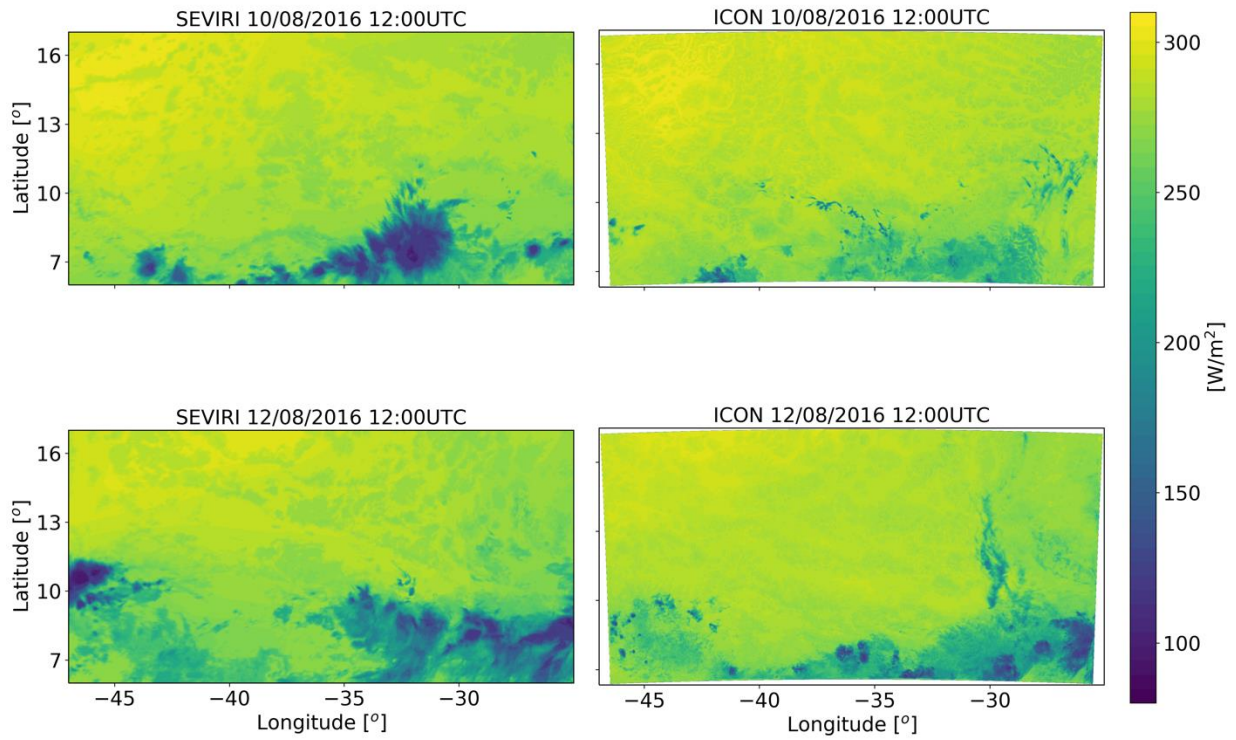
202 For comparing the outgoing longwave flux from the simulations and observations we use
203 imager data from the SEVIRI instrument onboard the Meteosat Second Generation (MSG)
204 geostationary satellite (Aminou, 2002). The outgoing longwave flux is calculated using the
205 Optimal Retrieval for Aerosol and Cloud (ORAC) algorithm (Sus et al. 2017; McGarragh, et
206 al. 2017). Cloud optical (thickness, effective radius, water path) and thermal (cloud top
207 temperature and pressure) properties are retrieved from ORAC using an optimal estimation-
208 based approach. These retrievals and reanalysis profiles of temperature, humidity and ozone
209 are then ingested into BUGSrad, a two-stream correlated-k broadband flux algorithm (Stephens
210 et al., 2001) that outputs the fluxes at the top and bottom of the atmosphere and shown to have
211 excellent agreement when applied to both active (CloudSat) and passive (Advanced Along
212 Track Scanning Radiometer) satellite sensors compared to Clouds and the Earth's Radiant
213 Energy System (Henderson et al. 2013; Stengel et al. 2019). In addition, off-line sensitivity
214 radiative transfer tests using vertical profiles from our model were conducted with BUGSrad
215 to identify the source of the differences in fluxes between clean and polluted conditions.



216

217 **Figure 1. Domain of the ICON simulations (red rectangle) overlaid on the August 2016 ECMWF era-**
218 **interim reanalysis (Dee et al., 2011) mean precipitation rate.**

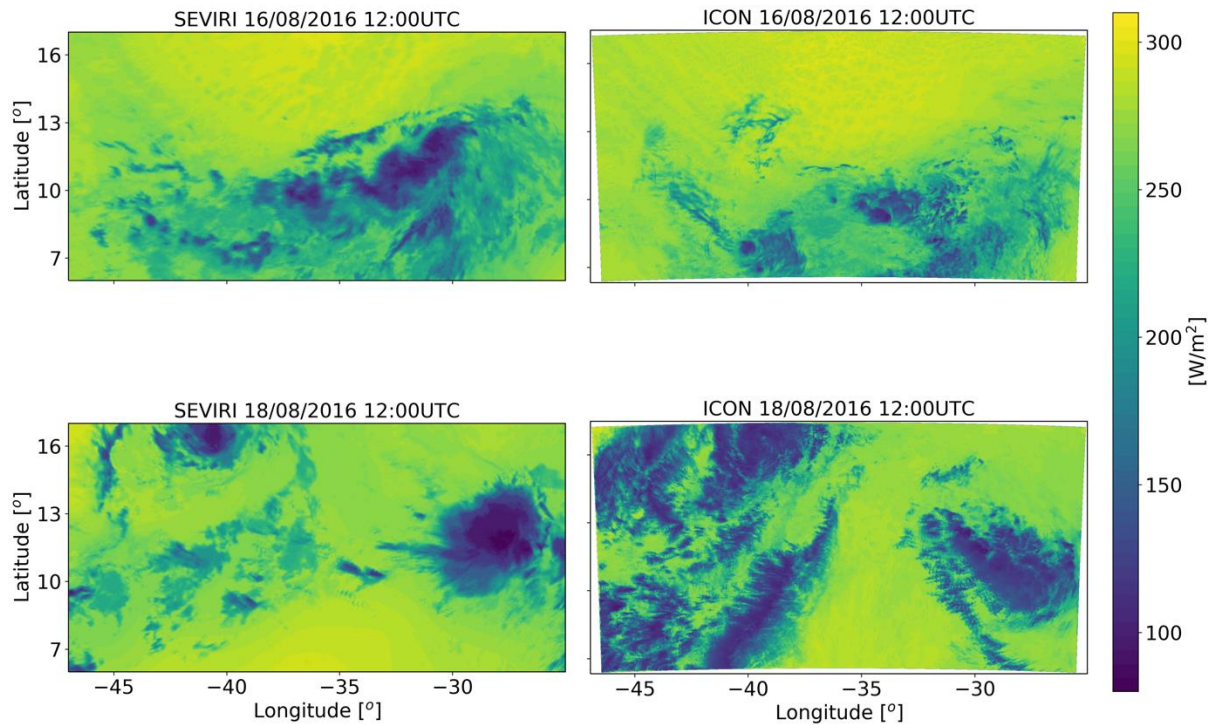
219



220
 221 **Figure 2. Outgoing longwave flux at the top of atmosphere at the initial stage (upper row) and the last stage**
 222 **(lower row – each average over 30 minutes) of the simulation of the shallow-cloud dominated case (10-**
 223 **12/08/2016) from geo-stationary satellite (SEVIRI-MSG – right column) and the ICON model simulation with**
 224 **CDNC of 20 cm^{-3} (left column).**

225

226



227

228 **Figure 3. similar to Figure 2 but for the deep-cloud dominated case (16-18/08/2016).**

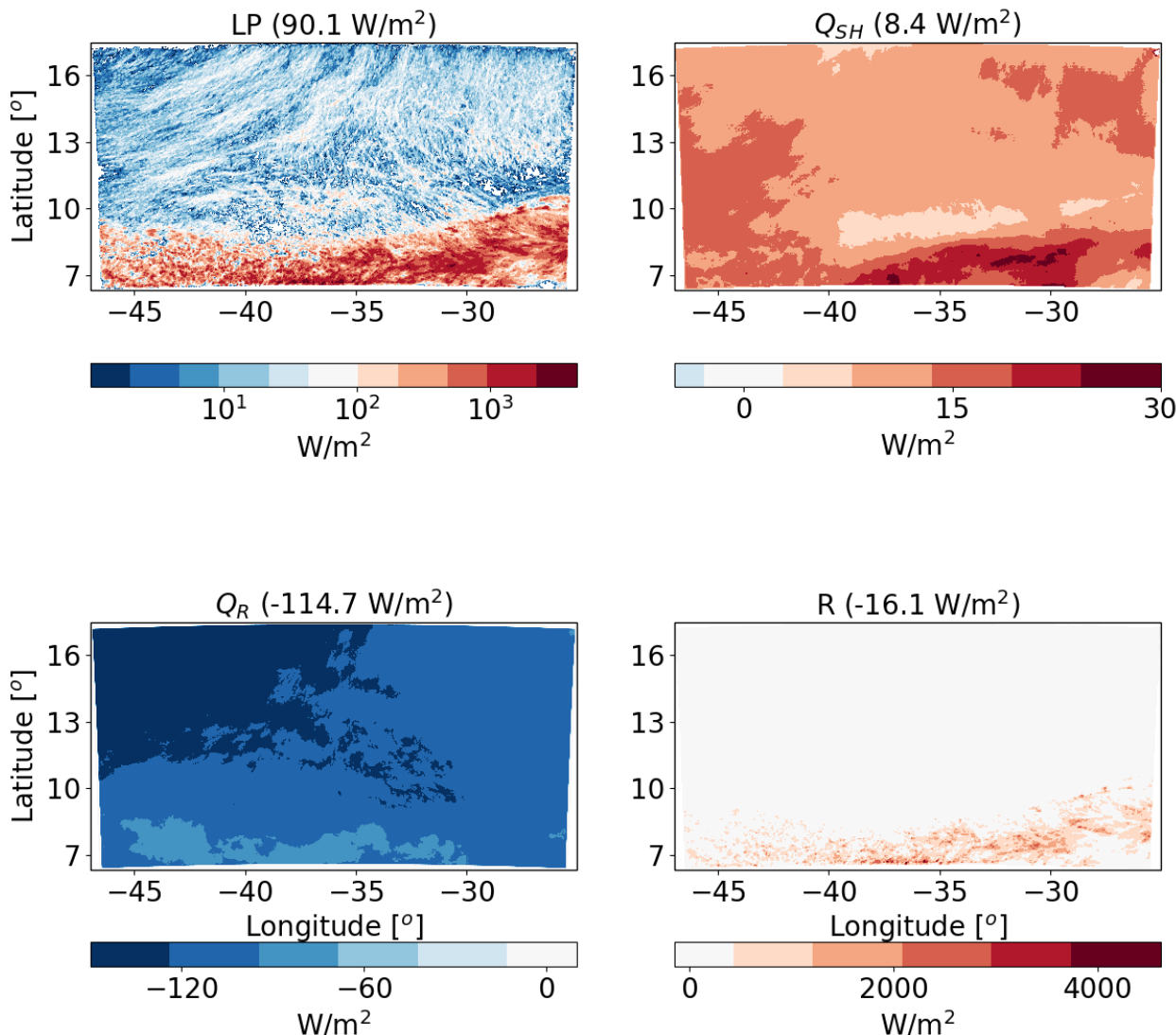
229 **Results**

230 **Shallow-cloud dominated case -10-12/08/2016**

231 We start with energy budget analysis of the shallow-cloud dominated case base simulations
 232 ($CDNC = 20 \text{ cm}^{-3}$). Figure 4 presents the time mean (over the two days simulation) of the
 233 different terms of the energy budget (Equation 1). As expected, LP dominates the warming of
 234 the atmosphere while Q_R dominate the cooling. The sensible heat flux (Q_{SH}) is positive (act to
 235 warm the atmosphere) but it is an order of magnitude smaller than the LP and Q_R magnitudes. In
 236 this shallow-cloud dominated case the radiative cooling of the atmosphere is significantly larger
 237 than the warming due to precipitation (mean of -114.7 W/m^2 compared to 90.1 W/m^2), hence the
 238 energy imbalance (R) is negative. Negative R means that there must be some convergence of dry
 239 static energy into the domain and/or decrease in the storage term, in this case it is mostly due to
 240 convergence of dry static energy.

241 We note that there is a significant difference in the spatial distribution of LP and Q_R (Jakob et al., 2019). While the Q_R is more uniformly distributed, the LP is mostly concentrated at the south part of the domain (where the deep convective clouds are formed) and it has a dotted structure. Locally, at the core of a deep convective clouds, the LP contribution can reach a few 1000 W/m^2 (1 mm/hr of precipitation is equivalent to 628 W/m^2), however, the vast majority of the domain

246 contributes very little in terms of LP . Q_R also presents some spatial structure in which there is a
 247 weak atmospheric cooling at the south part of the domain (the region of the deep convective
 248 clouds) and a strong cooling at the rest of the domain.

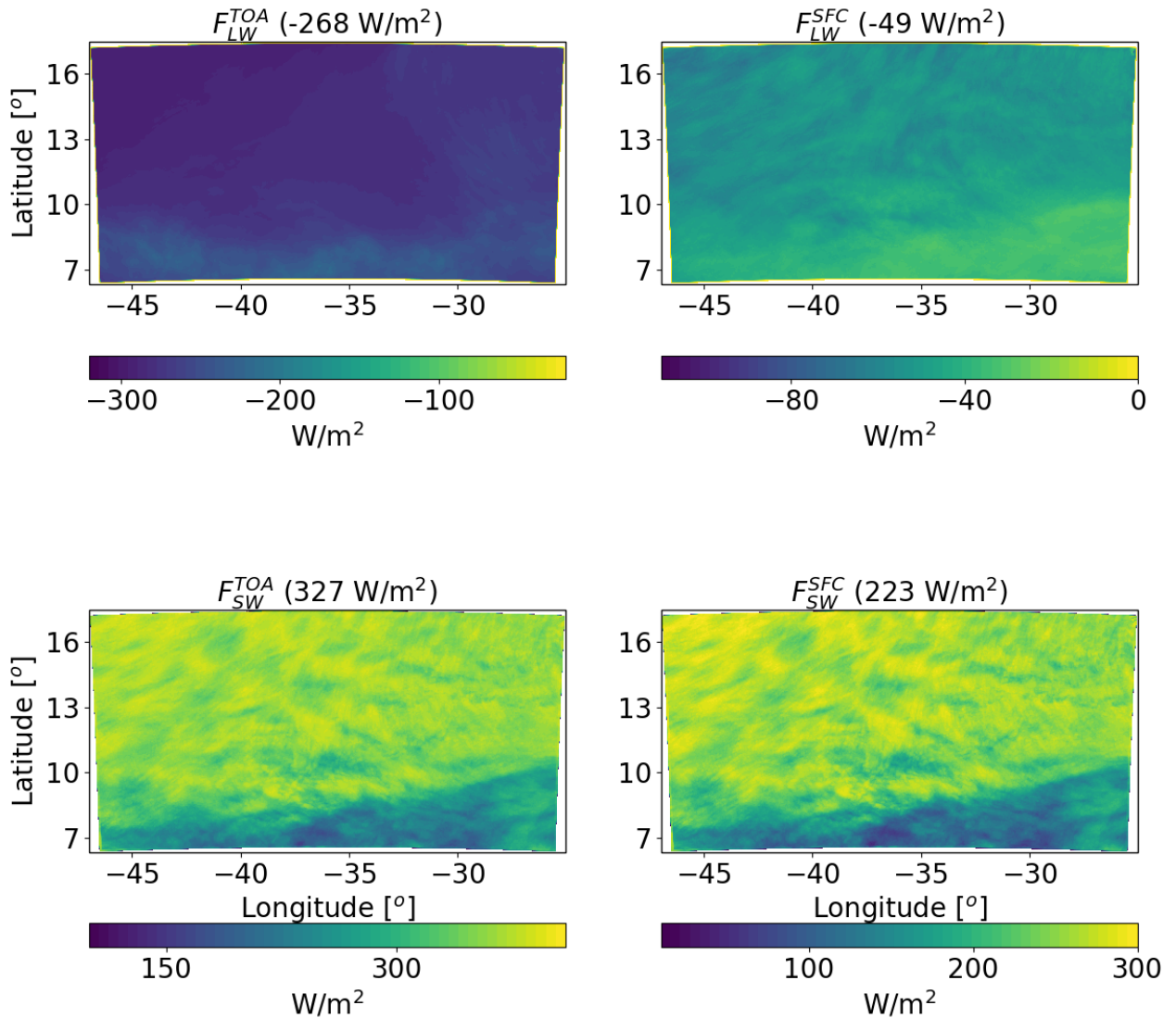


249
 250 **Figure 4. Spatial distribution of the time mean of the different terms of the energy budget for the ICON**
 251 **simulation of the shallow-cloud dominated case (10-12/08/2016) with $CDNC = 20 \text{ cm}^{-3}$. The terms that appear**
 252 **here are: LP - latent heat by precipitation, Q_{SH} - sensible heat flux, Q_R - atmospheric radiative warming, and**
 253 **R – the energy imbalance. The domain and time-mean value of each term appears in parenthesis.**

254
 255 For understanding the spatial structure of Q_R , next we examine the spatial distribution of the LW
 256 and SW radiative fluxes at the TOA and surface (Fig. 5). We note that the smaller radiative
 257 cooling in the region of deep clouds in the south of the domain is mostly contributed by a
 258 decrease in F_{LW}^{TOA} . The SW fluxes also demonstrate a strong south-north gradient, as the deep

259 convective clouds in the south are more reflective than the shallow trade cumulus (with the lower
 260 mean cloud fraction) in the rest of the domain.

261



262

263 **Figure 5. Spatial distribution of ICON simulated time-mean longwave (LW) and shortwave (SW) radiation**
 264 **fluxes at the top of atmosphere (TOA) and surface (SFC) for a simulation of the shallow-cloud dominated**
 265 **case (10-12/08/2016) with CDNC = 20 cm⁻³. The domain and time mean value of each term appears in**
 266 **parenthesis.**

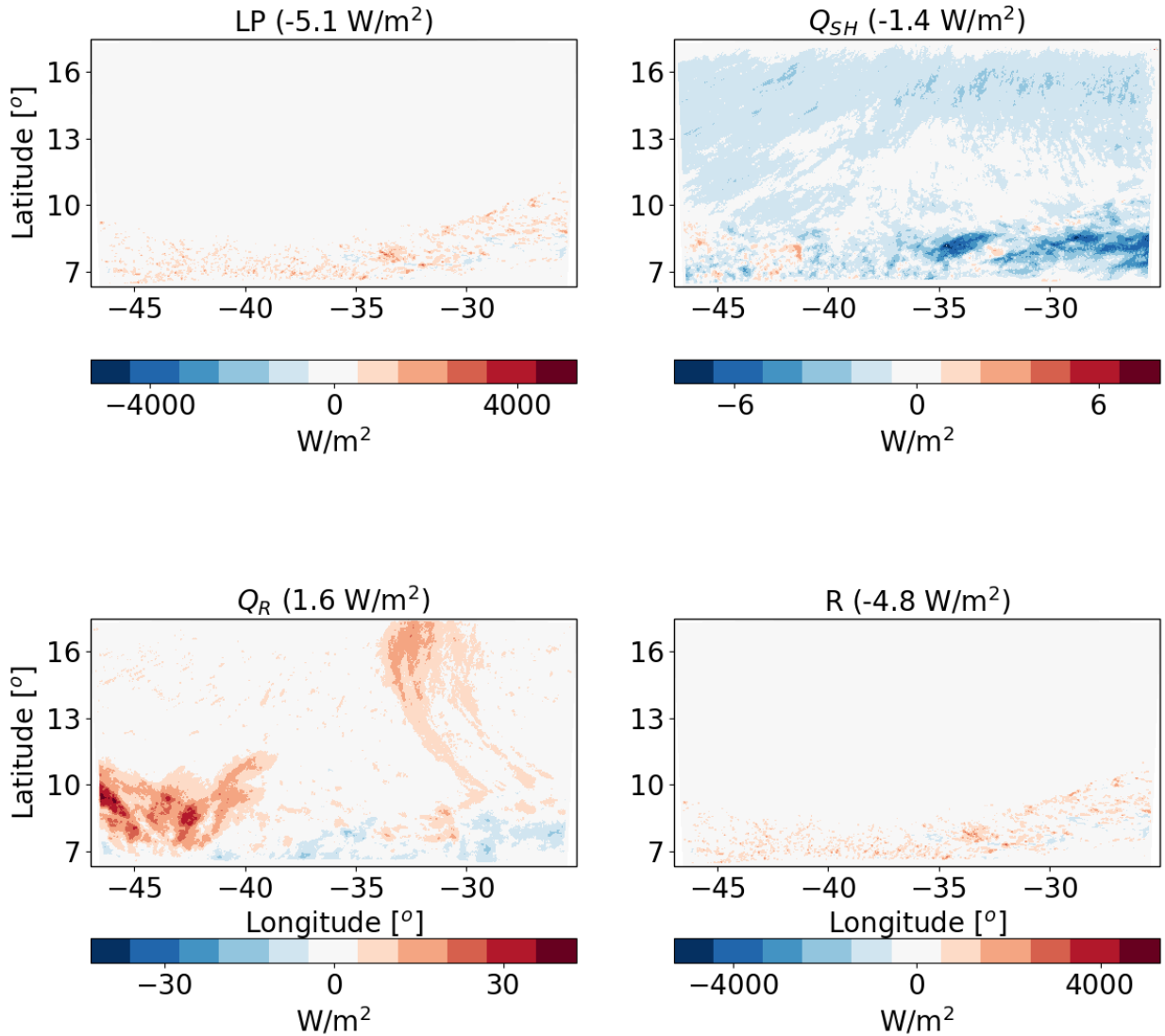
267

268 **Response to aerosol perturbation – shallow-cloud dominated case**

269 Next, we analyse the response of the atmospheric energy budget of this case to perturbations in
 270 CDNC. Figure 6 presents the differences in the different terms of the energy budget between a

271 polluted simulation ($CDNC = 200 \text{ cm}^{-3}$) and a clean simulation ($CDNC = 20 \text{ cm}^{-3}$). It
272 demonstrates that the LP differences between the different $CDNC$ scenarios contribute 5.1 W/m^2
273 less to warm the atmosphere in the polluted vs. the clean simulation. We note that this apparently
274 large effect is caused by a small, non-statistically significant, precipitation difference ($\sim 0.4 \text{ mm}$
275 over the two days of simulation - see Fig. 8 below). The strong sensitivity of the atmospheric
276 energy budget to small precipitation changes (recalling that 1 mm/hr is equivalent to 628 W/m^2)
277 exemplifies the caution one needs to take when looking on precipitation response in terms of
278 energy budget perspective. The Q_R differences lead to relative warming of the atmosphere of the
279 polluted case compared to the clean case by 1.6 W/m^2 . We note that most of the Q_R differences
280 are located in the south-west part of the domain. The Q_{SH} changes counteracts 1.4 W/m^2 of the
281 atmospheric warming by Q_R and so the end result is a deficit of 4.8 W/m^2 in the atmospheric
282 energy budget in the polluted simulation compared to the clean simulation. The decrease in the
283 Q_{SH} is driven by an increase in the near surface air temperature (see Fig. 8).

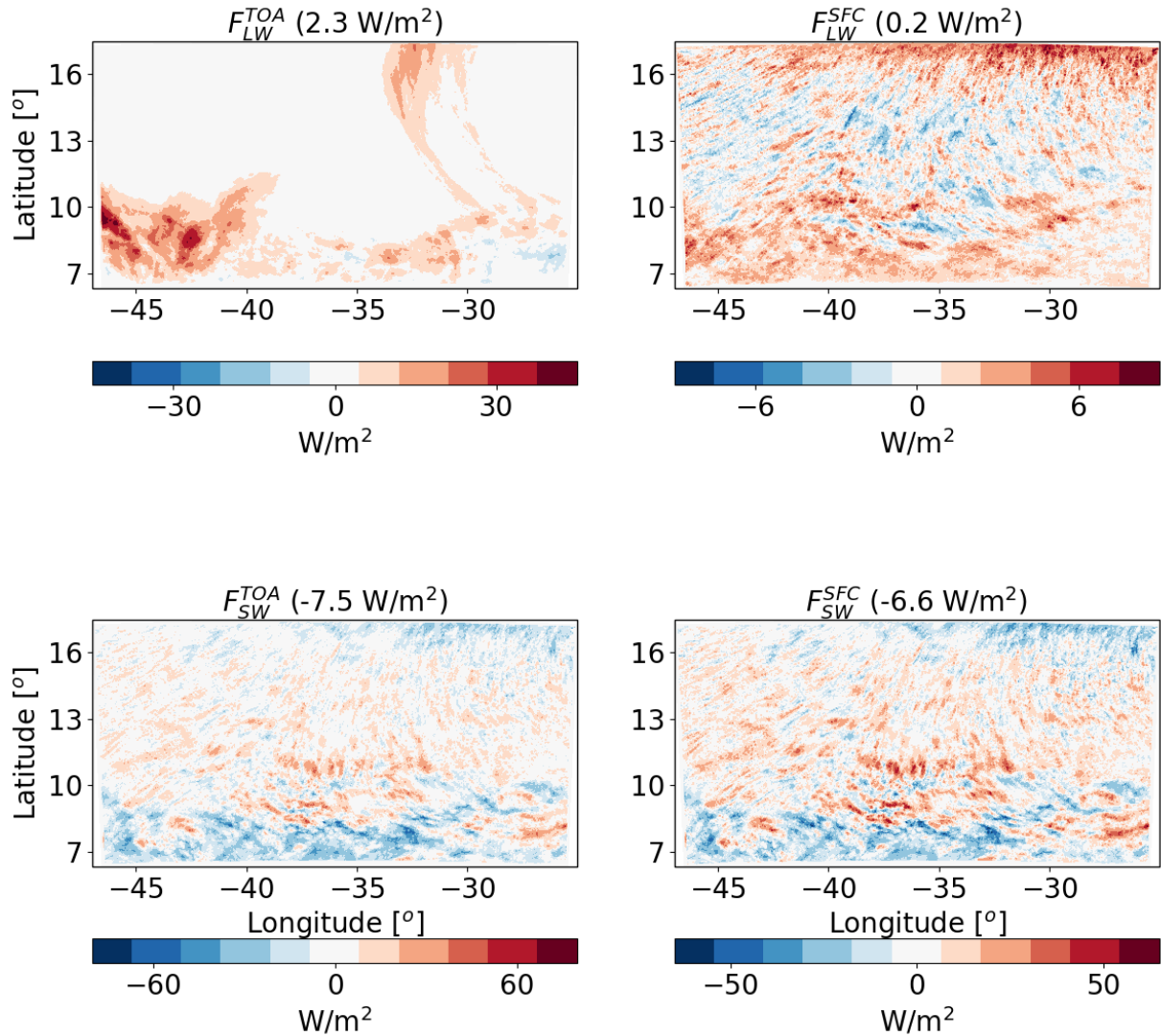
284



285
 286 **Figure 6.** The differences between polluted ($\text{CDNC} = 200 \text{ cm}^{-3}$) and clean ($\text{CDNC} = 20 \text{ cm}^{-3}$) ICON simulations
 287 of the time-mean terms of the energy budget for the shallow-cloud dominated case (10-12/08/2016). The terms
 288 that appears here are: LP - latent heat by precipitation, Q_{SH} - sensible heat flux, Q_R - atmospheric radiative
 289 warming, and R – the energy imbalance. The domain and time mean value of each term appears in
 290 parenthesis.

291 To understand the response of Q_R to the CDNC perturbation, we next examine the response of
 292 the different radiative fluxes. Figure 7 demonstrates that most of the relative atmospheric
 293 radiative heating in the polluted case compared to the clean case is contributed by changes in the
 294 F_{LW}^{TOA} fluxes. The changes in F_{LW}^{SFC} are an order of magnitude smaller. The SW fluxes change both
 295 at the TOA and SFC are larger than the F_{LW}^{TOA} changes, however, in terms of the atmospheric energy
 296 budget, they almost cancel each other out and the net SW atmospheric effect is only -0.9 W/m^2 .
 297 Most of the reduction in SW fluxes (both at TOA and the surface) comes from the deep
 298 convective regions in the south of the domain while the shallow cloud regions experience some

299 increase in SW fluxes. This can be attributed to the increase in deep convective cloud fraction
 300 and a decrease in the shallow cloud fraction with the increase in CDNC (see Fig. 9 below). The
 301 TOA net radiative effect for the entire system (as opposed to the atmospheric energy budget that
 302 take into consideration the surface radiative fluxes changes) is about -5.2 W/m^2 .



303
 304 **Figure 7.** The differences between polluted ($\text{CDNC} = 200 \text{ cm}^{-3}$) and clean ($\text{CDNC} = 20 \text{ cm}^{-3}$) ICON simulations
 305 of the time mean radiative longwave (LW) and shortwave (SW) fluxes at the top of atmosphere (TOA) and
 306 surface (SFC) for the shallow-cloud dominated case (10-12/08/2016). The domain and time mean value of
 307 each term appears in parenthesis.

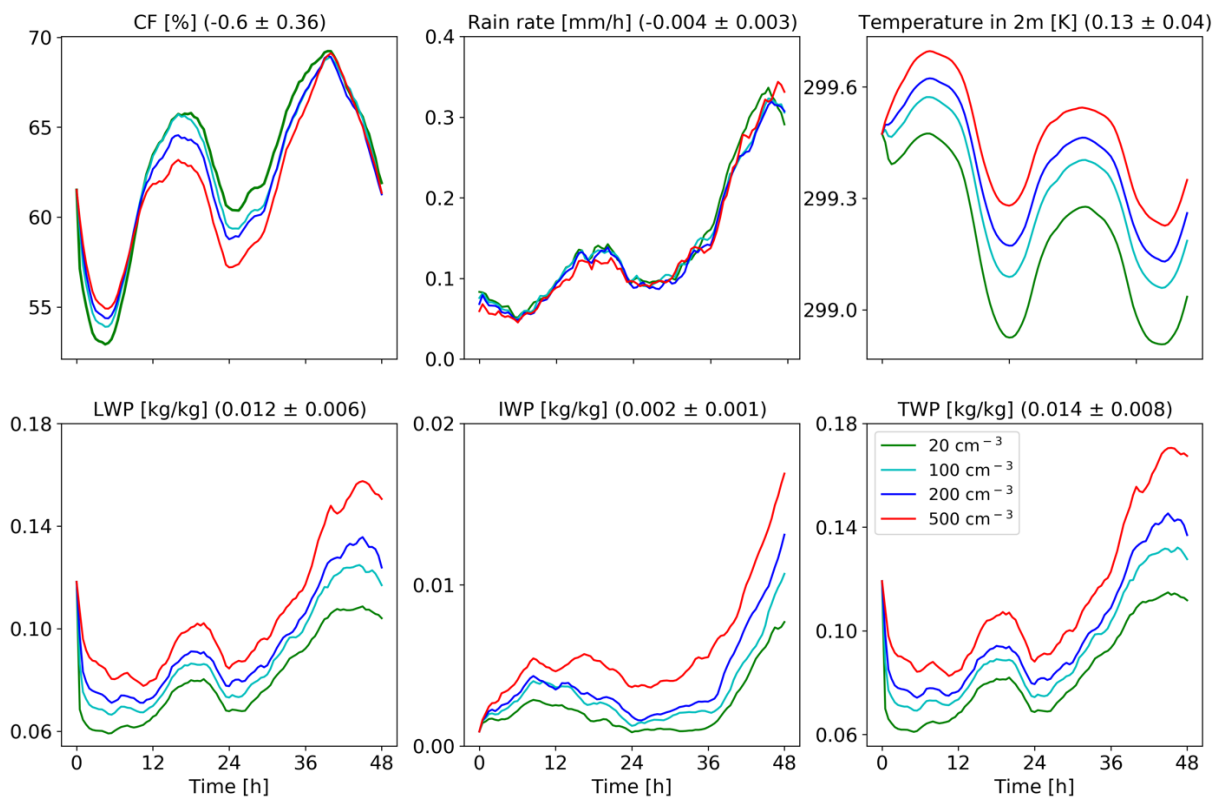
308
 309 The differences in the energy (Fig. 6) and radiation (Fig. 7) budgets between the clean and
 310 polluted cases shown above, could be explained by the differences in the cloud mean properties.
 311 Figure 8 presents the time evolution of some of the domain mean properties while Fig. 9 presents
 312 time and horizontal mean vertical profiles. To examine the robustness of the trends we add here

313 two more CDNC cases of 100 and 500 cm^{-3} (on top of the two that were examine above – 20 and
314 200 cm^{-3}). Figure 8 demonstrates that the domain mean cloud fraction (CF) generally decreases
315 with the increase in CDNC (except for the first ~10 hours of the simulations). Examining the
316 vertical structure of the CF response (Fig. 9), demonstrates that with the increase in CDNC there
317 is a reduction in the low level (below 800 mb) CF concomitantly with an increase in CF at the
318 middle and upper troposphere. The differences in rain rate between the different simulations are
319 small. However, both the liquid water path (LWP) and the ice water path (IWP) show a consistent
320 increase with CDNC. Accordingly, also the total water path (TWP), which is the sum of the LWP
321 and the IWP, substantial increases with CDNC. The vertical profiles of the different hydrometers
322 (Fig. 9) indicate, as expected, that the cloud droplet mass mixing ration (q_c - droplet with radius
323 smaller than 40 μm) increases with CDNC, while the rain mass mixing ratio (q_r - drops with
324 radius larger than 40 μm) decreases due to the shift in the droplet size distribution to smaller
325 sizes under larger CDNC conditions. As this case is dominated by shallow clouds, there exists
326 only a comparably small amount of ice mixing ration (q_i) (c.f. Fig. 17), but its concentration
327 increases with the CDNC increase. The combined effect of the increase in CDNC is to
328 monotonically increase the total water mixing ratio (q_t) above 800 mb (Fig. 9). The relative
329 increase in q_t with CDNC becomes larger at higher levels.

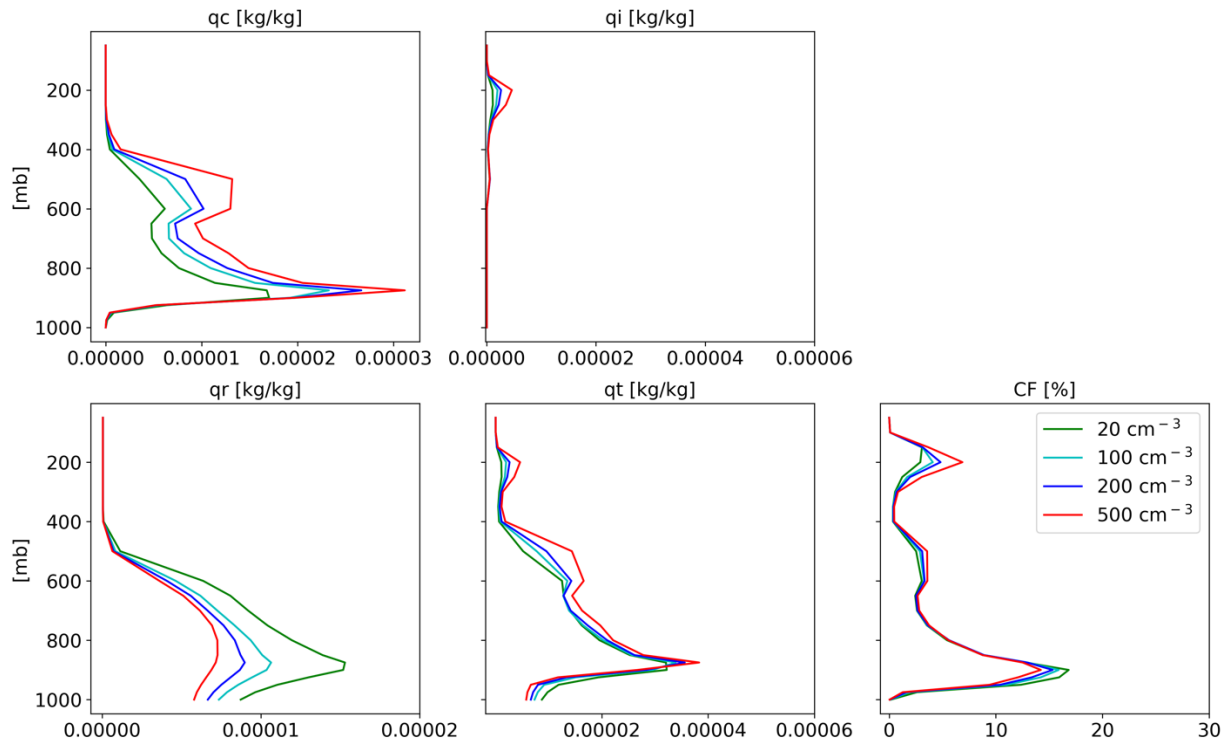
330 The increase in cloud water with increasing CDNC can explain both the reductions in the net
331 downward SW fluxes (both at TOA and surface) and the decrease in outgoing LW flux at TOA
332 (Fig. 7), as it results in more SW reflection concomitantly with more LW trapping in the
333 atmosphere (Koren et al., 2010). Another contributor to the SW flux reduction (more reflectance)
334 at the TOA is the Twomey effect (Twomey, 1977), while, the decrease in the low-level CF
335 compensates some of this effect. Here we present the outcome of these contradicting effects on
336 the SW fluxes, which shows a reduction at both the TOA and surface (Fig. 7). For estimating the
337 relative contribution of the Twomey effect compare to the cloud adjustments (CF and TWP
338 effects) to the SW flux changes, we have re-run the simulations with the Twomey effect turned
339 off (the radiation calculations do not consider the changes in effective radius between the
340 different simulations). It demonstrates that without the Twomey effect the TOA SW difference
341 is only -1.7 W/m^2 as compared to -7.5 W/m^2 with the Twomey effect, demonstrating the
342 predominant role of the Twomey effect. For estimating the relative contribution of the changes
343 in CF and water content to the SW flux changes we have conducted off-line radiative transfer
344 sensitivity tests. To quantify the water content radiative effect, we feed the same CF vertical
345 profile from the model into the offline radiative transfer model BUGSrad, while allowing the

346 water content vertical profile to change (and visa versa to compute the CF radiative effect). This
 347 approach demonstrates that the contribution from the small reduction in CF is negligible
 348 compared to the increased SW reflectance caused by the increased water content (the effect of
 349 the reduction in CF compensate only about 1% of the effect of the increase in the water content).

350 We also note a monotonic increase in the near surface temperature with CDNC (see also Fig. 10
 351 below). This trend can be explained by warm rain suppression with increasing CDNC that leads
 352 to less evaporative cooling (see the decrease in the total amount of water mass mixing ration just
 353 above the surface in Fig. 9, (Dagan et al., 2016; Albrecht, 1993; Seigel, 2014; Seifert and Heus,
 354 2013; Lebo and Morrison, 2014)). In addition, it was shown that under polluted conditions the
 355 rain drops below cloud base are larger, hence evaporating less efficiently (Lebo and Morrison,
 356 2014; Dagan et al., 2016). The increase in the near surface temperature drives the decrease in the
 357 Q_{SH} (Fig. 6).



358
 359 **Figure 8. Domain average properties as a function of time for the different CDNC simulations for the shallow-**
 360 **cloud dominated case. The properties that are presented here are: cloud fraction (CF), rain rate, temperature**
 361 **in 2 m, liquid water path (LWP – based on the cloud water mass, excluding the rain mass for consistency**
 362 **with satellite observations), ice water path (IWP) and total water path (TPW = LWP + IWP). For each**
 363 **property, the mean difference between all combinations of simulations, normalized to a factor 5 increase in**
 364 **CDNC, and its standard deviation appear in parenthesis.**



366

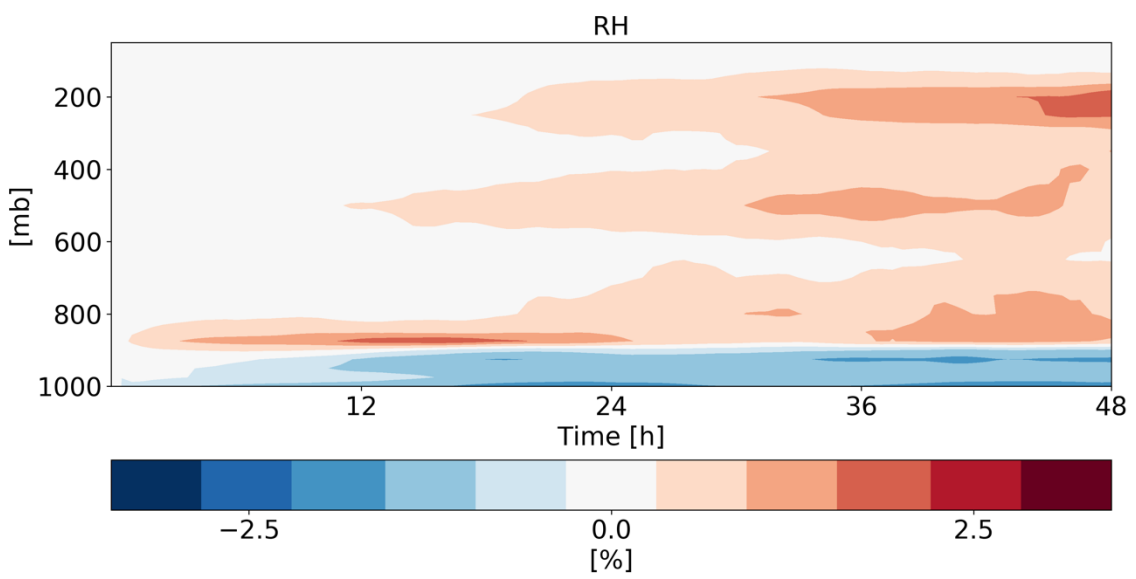
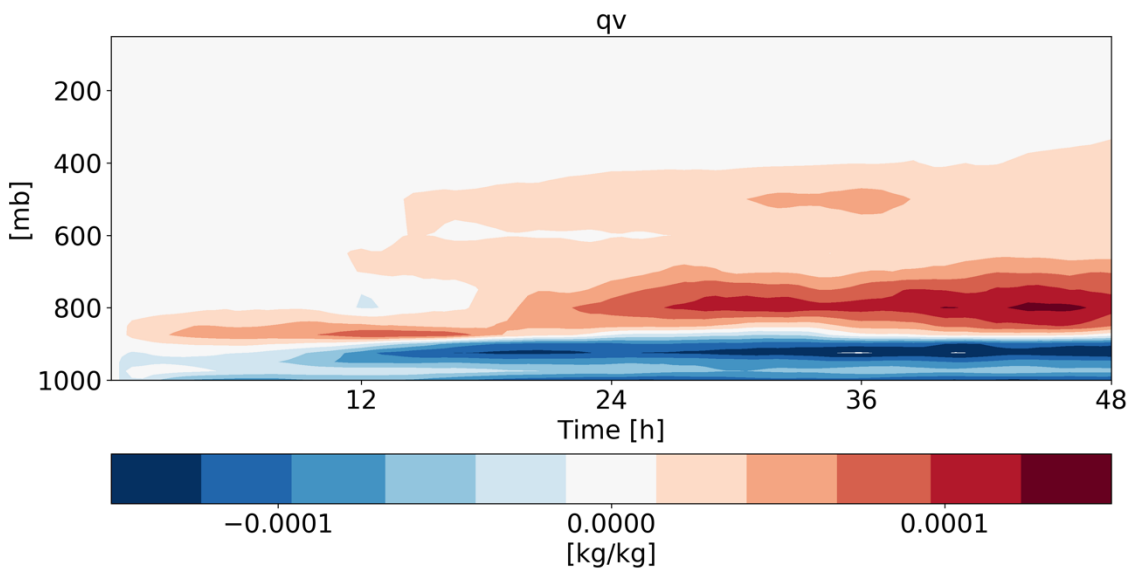
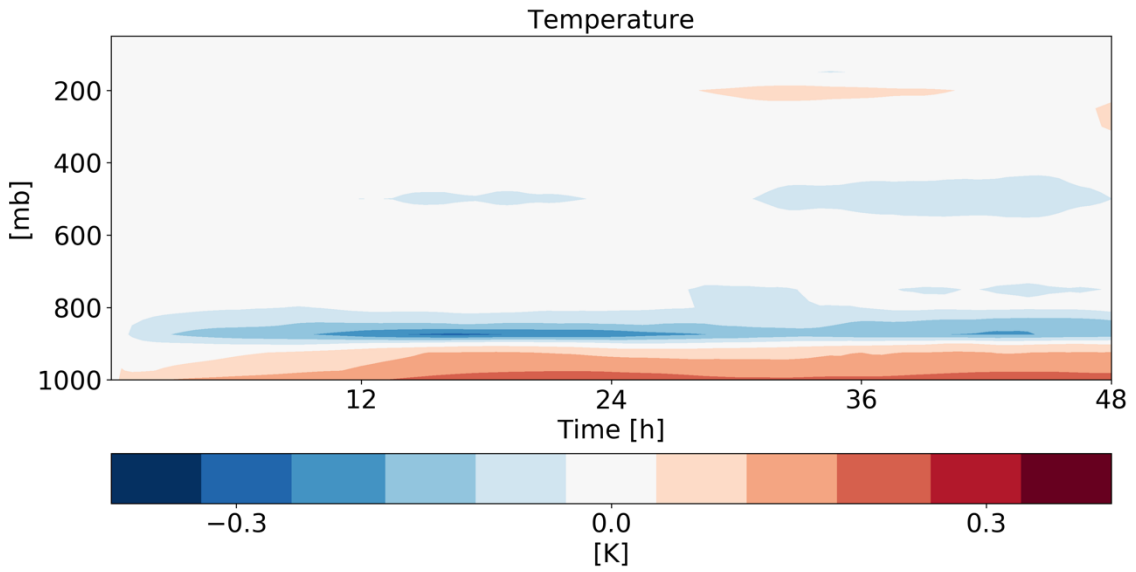
367 **Figure 9. Domain and time average vertical profiles for the different CDNC simulations for the shallow-cloud**
 368 **dominated case. The properties that are presented here are: cloud droplet mass mixing ratio (q_c – for clouds’**
 369 **droplets with radius smaller than $40\ \mu\text{m}$), ice mass mixing ratio (q_i), rain mass mixing ratio (q_r - for clouds’**
 370 **drops with radius larger than $40\ \mu\text{m}$), total water mass mixing ratio ($q_t = q_c + q_i + q_r$), and cloud fraction (CF).**
 371 **The x-axis ranges are identical as for the deep-cloud dominated case – Fig. 17.**

372

373 In addition to the clouds’ effect on the radiation fluxes, changes in humidity could also contribute
 374 (Fig. 10). We note that increase in CDNC leads to increase in relative humidity (RH) and specific
 375 humidity (q_v) at the middle and upper troposphere without a significant temperature change. The
 376 increased humidity at the upper troposphere would act to decrease the outgoing LW flux, similar
 377 to the effect of the increased ice content in the upper troposphere (Fig. 9). However, sensitivity
 378 studies with off-line radiative transfer calculations using BUGSrad demonstrate that the vast
 379 majority (more than 99%) of the different in F_{LW}^{TOA} between clean and polluted conditions emerges
 380 from the cloudy skies (rather than clear-sky), suggesting that the effect of the increased ice
 381 content at the upper troposphere dominates.

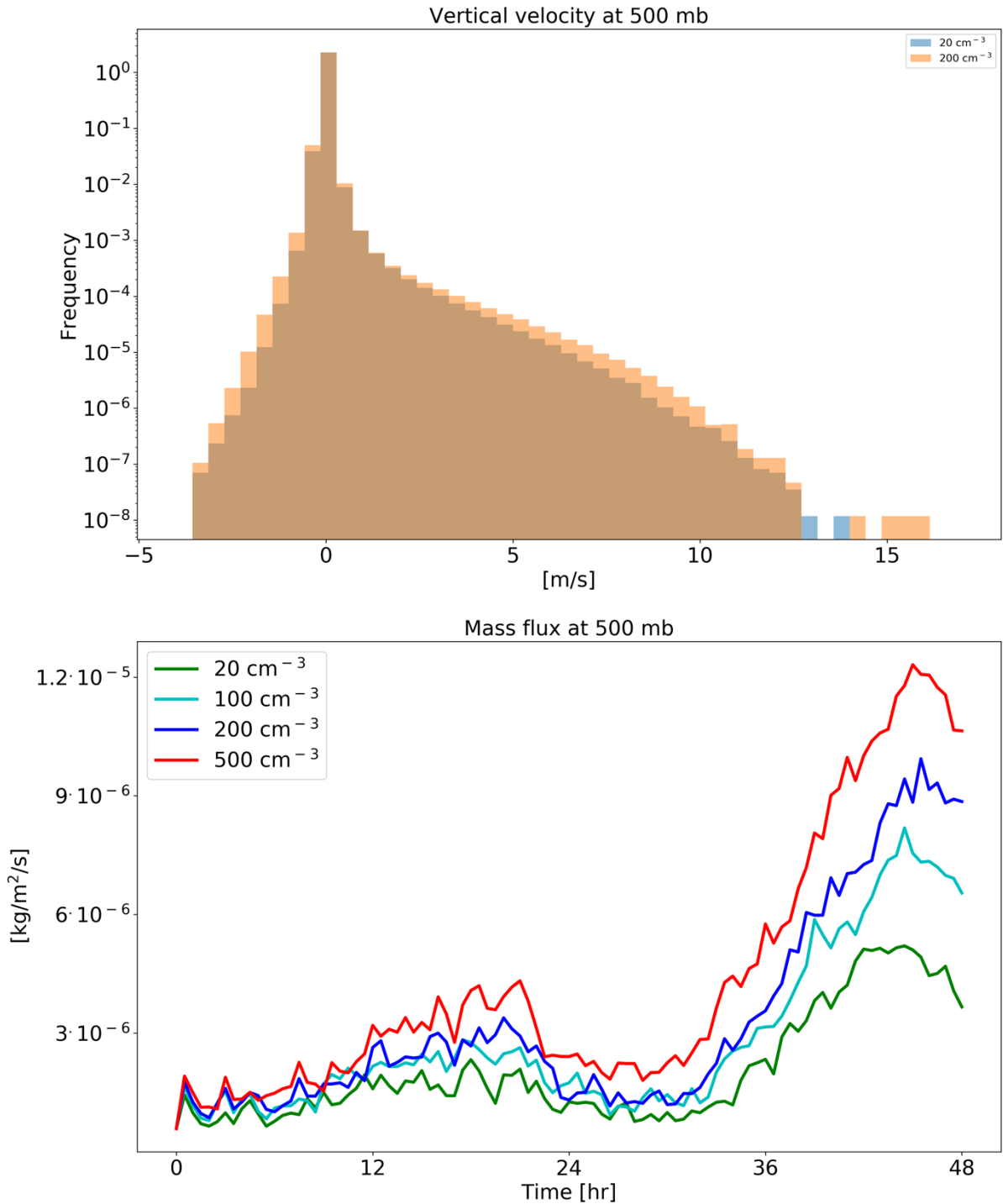
382 Both the increase in water vapor and ice content in the upper troposphere are driven by an
 383 increase in upward water (liquid and ice) mass flux with increasing CDNC (Fig. 11). An increase

384 in mass flux could be caused by an increase in vertical velocities and/or by an increase in cloud
385 (or updraft) fraction and/or by an increase in cloud water content. In our case, the increases in
386 mass flux is driven partially by the small increase in vertical velocity (especially for updraft
387 between 5 and 10 m/s – Fig. 11), partially by the small increase in cloud fraction at this level (Fig.
388 9) and mostly due to the larger water mass mixing ratio (Fig. 9) that leads to an increase in mass
389 flux even for a given vertical velocity. The increased relative humidity at the upper troposphere,
390 further increases the ice particle lifetime at these levels (in addition to the microphysical effect
391 (Grabowski and Morrison, 2016)) as the evaporation rate decreases. In addition, the differences
392 in the thermodynamics evolution between the different simulations (Fig. 10) demonstrate drying
393 and warming of the boundary layer with increasing CDNC, due to reduction in rain evaporation
394 below cloud base and deepening of the boundary layer (Dagan et al., 2016; Lebo and Morrison,
395 2014; Seifert et al., 2015; Spill et al., 2019). The drying of the boundary layer could explain the
396 reduction in the low cloud fraction (Fig. 9 (Seifert et al., 2015)).



398 **Figure 10. Time-height diagrams of the differences in the domain mean temperature, specific humidity (qv)**
 399 **and relative humidity (RH) vertical profiles between polluted (CDNC = 200 cm⁻³) and clean (CDNC = 20 cm⁻³)**
 400 **simulations for the shallow-cloud dominated case (10-12/08/2016).**

401



402

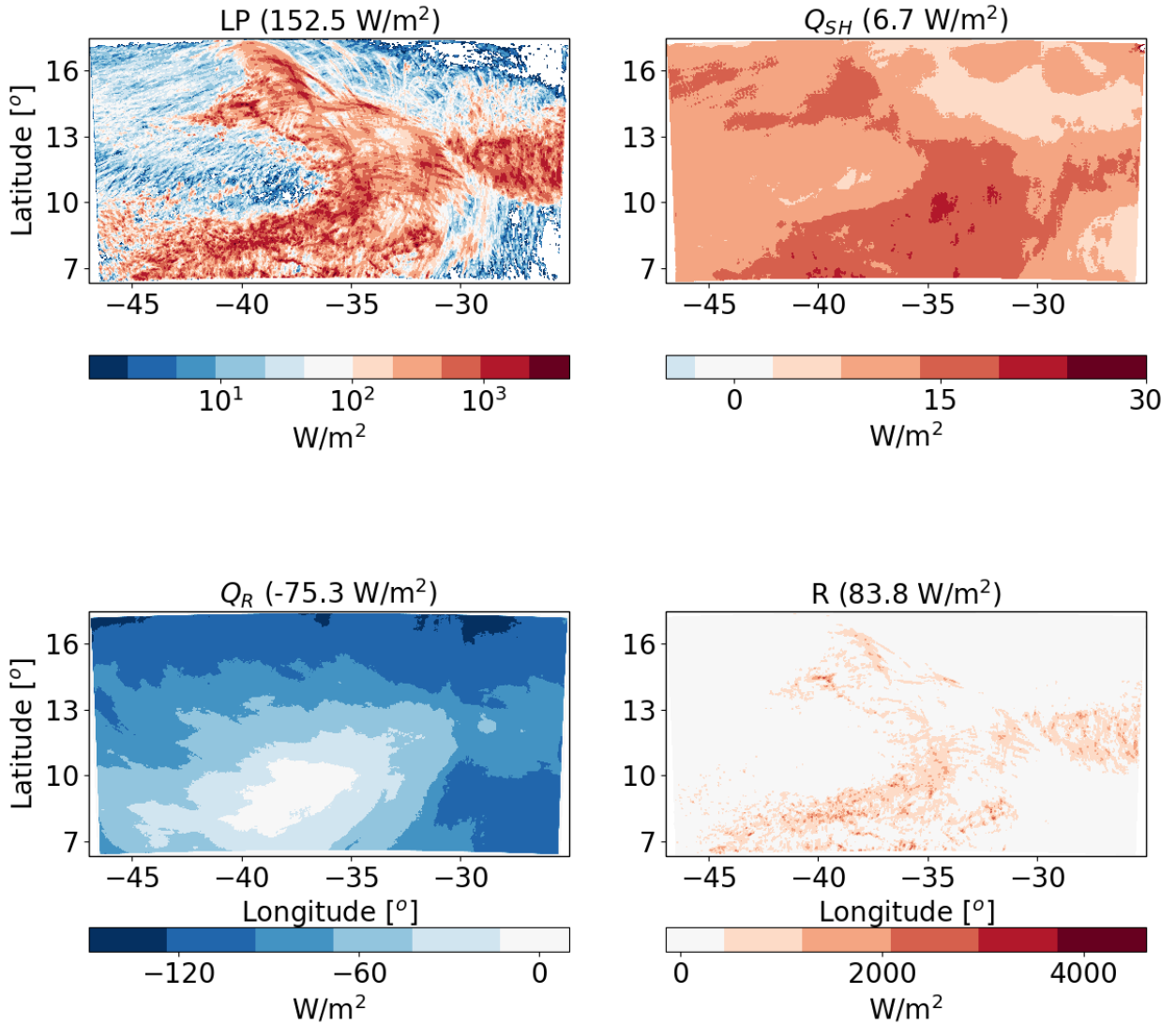
403 **Figure 11. histograms of ICON simulated vertical velocity at the level of 500 mb for a clean (CDNC = 20 cm⁻³)**
 404 **and polluted (CDNC = 200 cm⁻³) simulations (upper), and the time evolution of the net upwards water**
 405 **(liquid and ice) mass flux (lower) for the different CDNC simulations for the shallow-cloud dominated case**

406 (10-12/08/2016). The 500 mb level is chosen as it represents the transition between the warm part to the cold
407 part of the clouds. In the histogram only two simulations are presented for clarity.

408

409 **Deep-cloud dominated case -16-18/08/2016**

410 Next, we analyse the atmospheric energy budget for the deep-cloud dominated case (Fiona
411 tropical storm – Fig. 12). As opposed to the shallow-cloud dominated case, in this case the LP
412 contribution dominates over the radiative cooling and hence the energy imbalance R is positive
413 and large, suggesting divergence of dry static energy out of the domain. This difference in the
414 base line atmospheric energy budget between the different cases simulated here, enable an
415 examination of the aerosol effect on the atmospheric energy budget under contrasting initial
416 conditions. As in the shallow-cloud dominated case, the Q_R values varies between small values
417 (especially at the regions that were mostly covered by deep clouds) to larger negative values
418 (dominated at the regions that were covered by shallow clouds). The Q_{SH} is positive and an order
419 of magnitude smaller than the Q_R and LP , similar to the shallow-cloud dominated case.



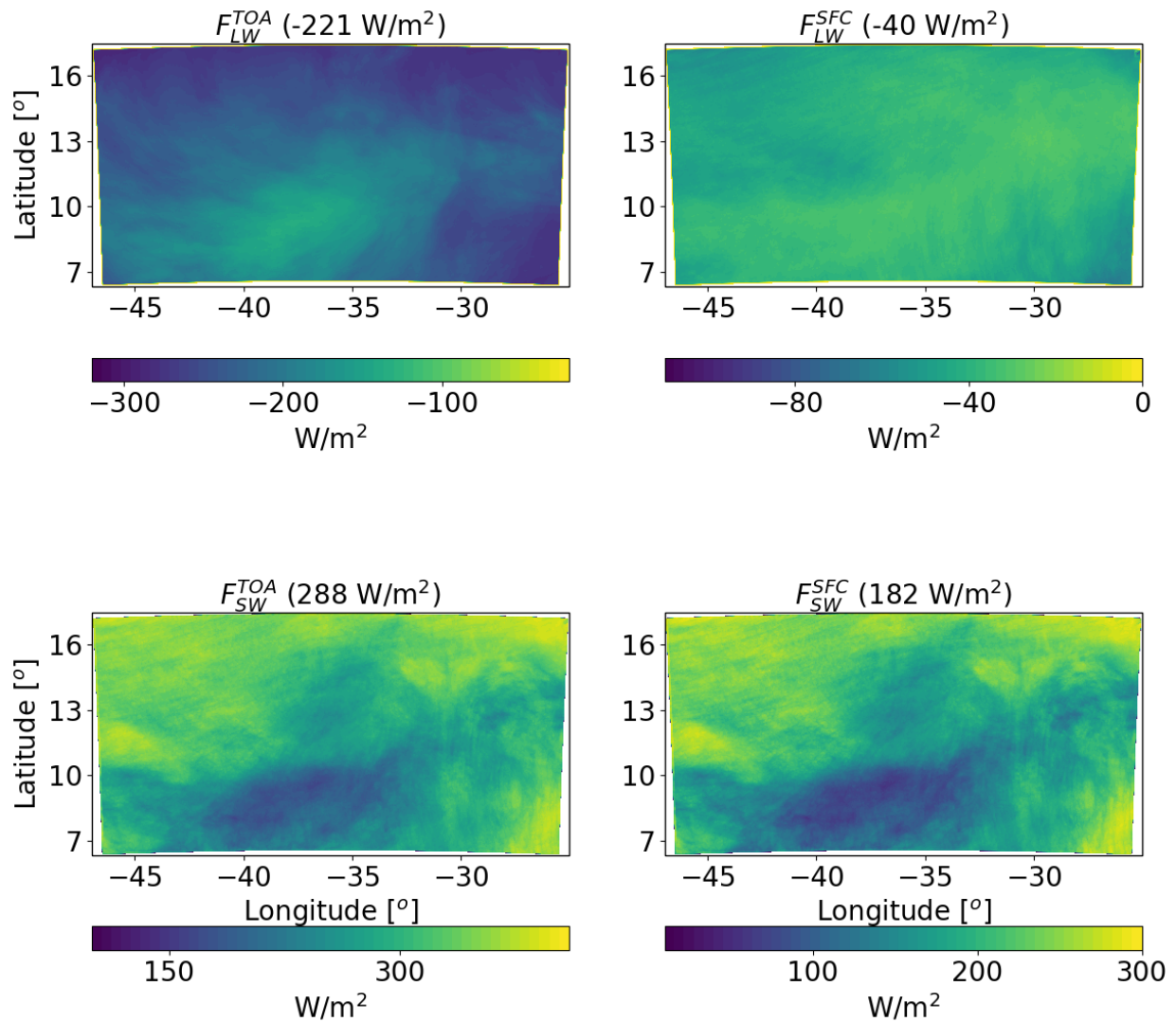
420

421 **Figure 12.** Spatial distribution of the time mean of the different terms of the energy budget for the ICON
 422 simulation of the deep-cloud dominated case (16-18/08/2016) with $CDNC = 20 \text{ cm}^{-3}$. The terms that appear
 423 here are: LP - latent heat by precipitation, Q_{SH} - sensible heat flux, Q_R - atmospheric radiative warming, and
 424 R – the energy imbalance. The domain and time-mean value of each term appears in parenthesis.

425

426 Further examination of the radiative fluxes (Fig. 13) demonstrates again the resemblance in the
 427 spatial structure between Q_R and F_{LW}^{TOA} . As compared to the shallow-cloud dominated case, since
 428 the clouds are more opaque and cover larger fraction of the sky, there is a decrease in the
 429 magnitude of all fluxes (in different amount). For example, F_{SW}^{SFC} is lower by 41 W/m^2
 430 (representing larger SW reflectance back to space) and the magnitude of F_{LW}^{TOA} by 47 W/m^2 as
 431 compare to the shallow-cloud dominated case. The combined effect of the radiative flux

432 differences between the two cases is a decrease of the atmospheric radiative cooling by 39.6
 433 W/m^2 (-114.7 compare with -75.3 W/m^2 – see Figs. 5 and 13).

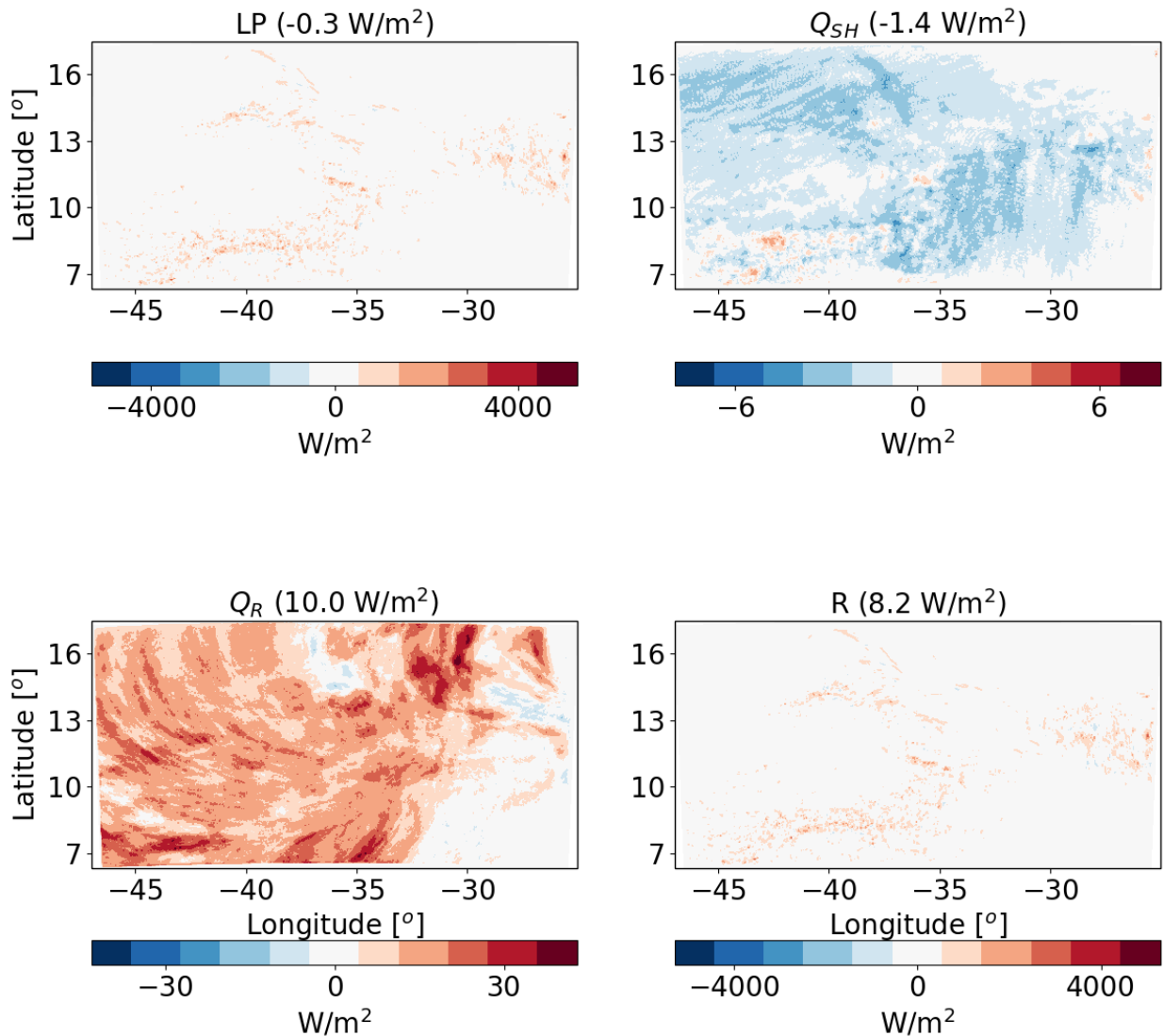


434
 435 **Figure 13. Spatial distribution of ICON simulated time-mean longwave (LW) and shortwave (SW) radiation**
 436 **fluxes at the top of atmosphere (TOA) and surface (SFC) for a simulation of the deep-cloud dominated case**
 437 **(16-18/08/2016) with $\text{CDNC} = 20 \text{ cm}^{-3}$. The domain and time mean value of each term appears in parenthesis.**

438
 439 **Response to aerosol perturbation – deep-cloud dominated case**

440 For the deep-cloud dominated case, an increase in CDNC results in a decrease in LP by -0.3
 441 W/m^2 . Again, this difference is due to a non-statistically significant precipitation changes (see
 442 also Fig. 16 below). A similar Q_{SH} decrease as in the shallow-cloud dominated case is observed
 443 in the deep-clouds dominated case (see Figs. 14 and 6). The predominant difference in the

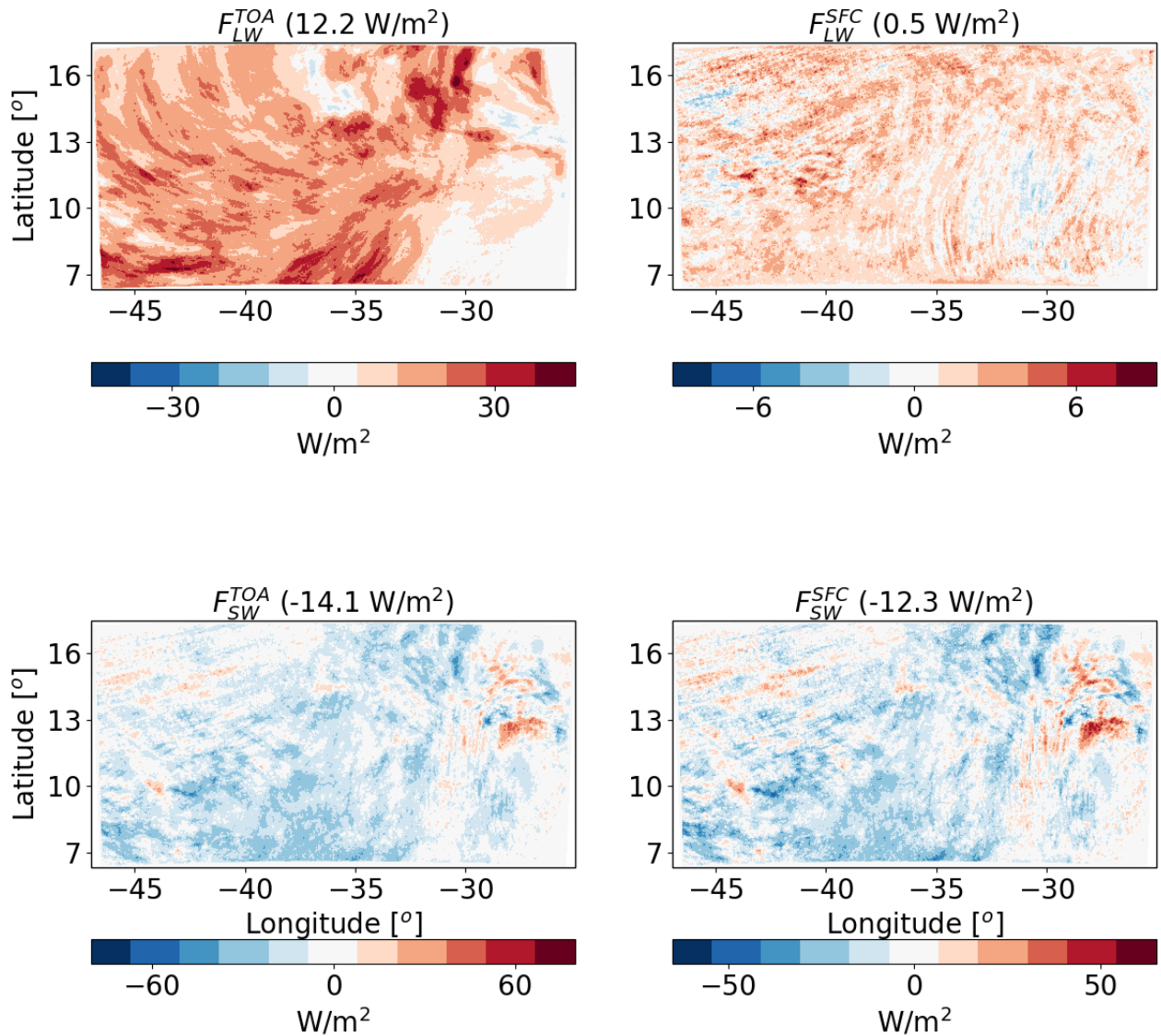
444 response between the two cases is in Q_R , which increases much more in the deep-cloud dominated
 445 case: 10.0 W/m^2 (Fig. 14) compared with 1.6 W/m^2 in the shallow-cloud dominated case (Fig.
 446 6).



447
 448 **Figure 14.** The differences between polluted (CDNC = 200 cm⁻³) and clean (CDNC = 20 cm⁻³) ICON
 449 simulations of the time-mean terms of the energy budget for the deep-cloud dominated case (16-18/08/2016).
 450 The terms that appears here are: LP - latent heat by precipitation, Q_{SH} - sensible heat flux, Q_R - atmospheric
 451 radiative warming, and R - the energy imbalance. The domain and time mean value of each term appears in
 452 parenthesis.

453
 454 The large increase in Q_R is caused mostly by the increase in F_{LW}^{TOA} (which becomes less negative
 455 i.e. less outgoing LW radiation under polluted conditions – Fig. 15). The CDNC effect on F_{LW}^{SFC}
 456 has a much smaller magnitude. The SW fluxes changes are substantial (-14.1 W/m^2 at TOA and

457 -12.3 W/m² at the surface), however, in terms of the atmospheric energy budget, since clouds do
 458 not absorb much in the SW, the TOA and surface changes almost cancel each other out and the
 459 net effect is only ~1.8 W/m² atmospheric radiative cooling (which decrease some of the LW
 460 warming). The net TOA total (SW+LW) radiative flux change is about -1.9 W/m². The trends in
 461 the mean cloud properties (Figs. 16 and 17 below) can explain this large radiative response.



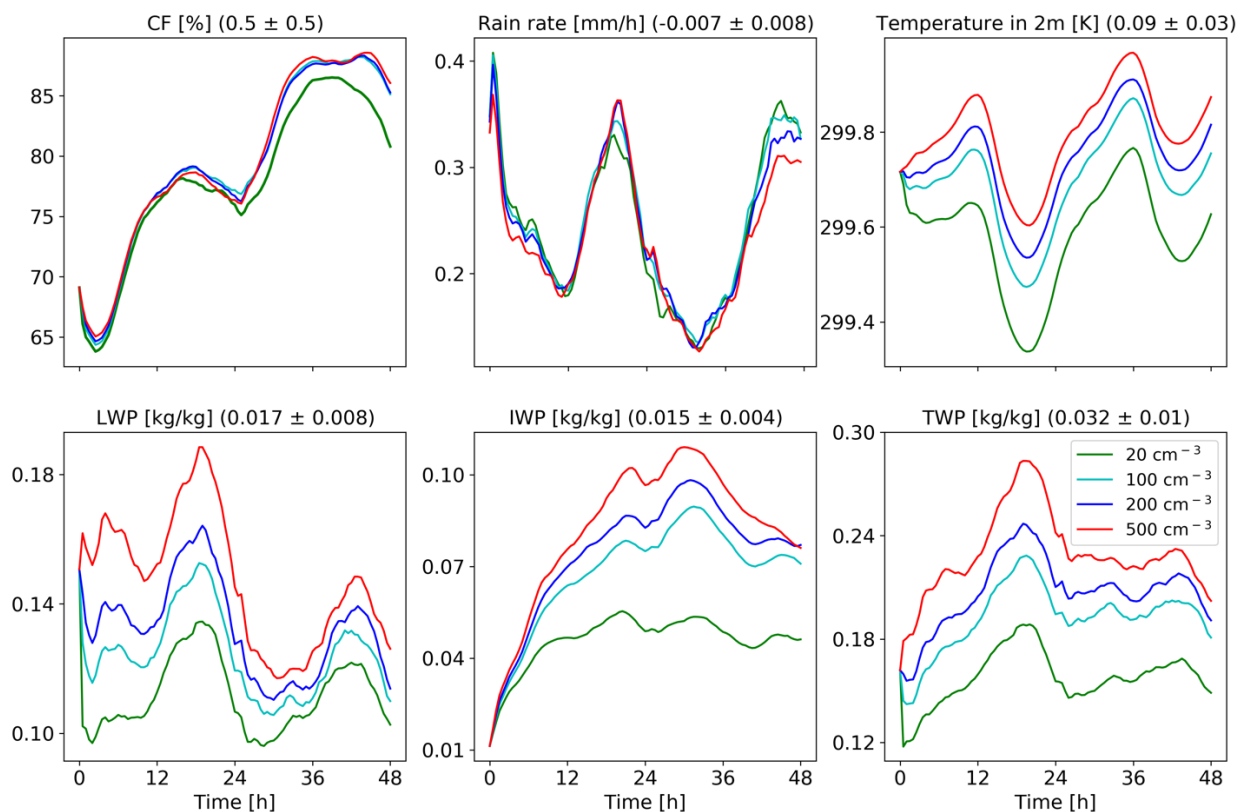
462
 463 **Figure 15.** The differences between polluted (CDNC = 200 cm⁻³) and clean (CDNC = 20 cm⁻³) ICON
 464 simulations of the time mean radiative longwave (LW) and shortwave (SW) fluxes at the top of atmosphere
 465 (TOA) and surface (SFC) for the deep-cloud dominated case (16-18/08/2016). The domain and time mean
 466 value of each term appears in parenthesis.

467

468 Figure 16 presents some of the domain mean properties as a function of time for the deep-cloud
469 dominated case. It demonstrates an increase in CF with CDNC which is more significant during
470 the second day of the simulation. This is opposite to the CF reduction in the shallow-cloud
471 dominated case (Fig. 8). It also demonstrates a very significant increase in LWP and, even more
472 (in relative terms), in IWP and thus also in TWP. The increase in CF and water content can
473 explain the decrease in SW fluxes both at TOA and surface (Fig. 15) as more SW is being
474 reflected back to space. The larger SW reflection under increased CDNC is also contributed to
475 by the Twomey effect (Twomey, 1977). Re-running the simulations without the Twomey effect
476 result in 9.6 W/m² reduction in the TOA SW flux as compare to 14.1 W/m² with the Twomey
477 effect on. We note that the relative role of the Twomey effect (compare to the cloud adjustments
478 – CF and TWP) is larger in the shallow-cloud dominated case as compared to the deep-cloud
479 dominated case (-14.1 W/m² and -9.6 W/m² for simulations with and without the Twomey effect
480 in the deep-cloud dominated case, compare to -7.5 W/m² and -1.7 W/m² in the shallow-cloud
481 dominated case, respectively). However, it should be noted that the Twomey effect due to
482 changes in the ice particles size distribution was not considered. In this case, unlike in the
483 shallow-cloud dominated case, the three contributions to the SW changes (CF, Twomey and
484 LWP/IWP, e.g. (Goren and Rosenfeld, 2014)) all contribute to the SW flux reduction (Fig. 15
485 presents the results of all contributors). Off-line sensitivity tests demonstrate that the relative
486 contribution of the water content and the CF to the increase in SW reflectance is roughly $\frac{3}{4}$ and
487 $\frac{1}{4}$, respectively.

488 The vertical profile changes with CDNC (Fig. 17) demonstrate a consistent picture of a decrease
489 in CF in low clouds and a significant increase in CF and liquid and ice content at the mid and
490 upper troposphere. The CF increase at the upper troposphere, and especially the increase in the
491 ice content, can explain the decrease in the outgoing LW radiation (Fig. 15). The increase in ice
492 content at the upper troposphere is in agreement with recent observational studies (Gryspeerd et
493 al., 2018; Sourdeval et al., 2018; Christensen et al., 2016). Analysis of the upward water mass
494 flux from the warm to the cold part of the clouds (at 500 mb) in the different simulations (Fig.
495 19), demonstrates a substantial increase with the increase in CDNC (Chen et al., 2017), which
496 occurs due to the increase in the water content (Fig. 17) and the delay in the rain formation to
497 higher levels (Heikenfeld et al., 2019), even without a large change in the vertical velocity or
498 cloud fraction at this level (Fig.17). Similar to the shallow-cloud dominated case (Fig. 8), the
499 near surface temperature monotonically increases with CDNC, while the effect on the mean rain
500 rate is small.

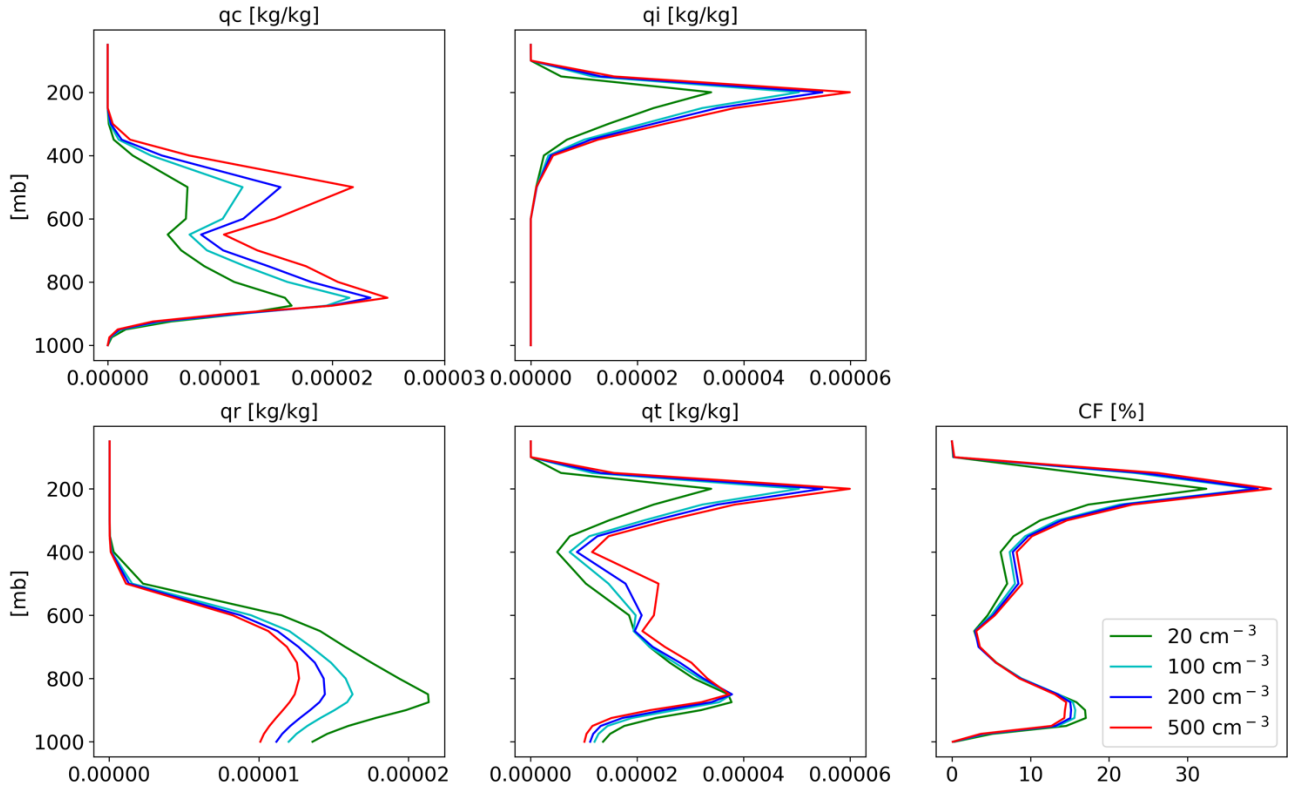
501 The differences in the thermodynamic evolution between polluted and clean conditions for this
 502 case (Fig. 18), demonstrate the same trend as in the shallow-cloud dominated case (Fig. 10).
 503 Here again, we note an increase in the humidity at the mid and upper troposphere, that contribute
 504 to the reduction in the outgoing LW flux. The deepening, drying and warming of the boundary
 505 layer are observed in this case as well. Both the increase in humidity at the mid-upper troposphere
 506 and the deepening of the boundary layer (Seifert et al., 2015) could cause a reduction of the
 507 outgoing LW flux. To distinguished the effect of clouds and humidity at the different levels on
 508 the outgoing LW flux, we have conducted sensitivity off-line radiative transfer calculations using
 509 BUGSrad. As in the shallow-cloud dominated case, the difference in outgoing LW flux between
 510 clean and polluted conditions primarily emerges from the CDNC effect on clouds. The small
 511 remaining effect of the clear sky ($\sim 0.2 \text{ W/m}^2$) is contributed by the change in the humidity at the
 512 mid and upper troposphere rather than by the deepening of the boundary layer (which would lead
 513 to LW emission from lower temperatures and is expected to be more significant under lower free
 514 troposphere humidity conditions).



515
 516 **Figure 16. Domain average properties as a function of time for the different CDNC simulations for the deep-**
 517 **cloud dominated case. The properties that are presented here are: cloud fraction (CF), rain rate, temperature**
 518 **in 2 m, liquid water path (LWP – based on the cloud water mass, excluding the rain mass for consistency**
 519 **with satellite observations), ice water path (IWP) and total water path (TPW = LWP + IWP). For each**

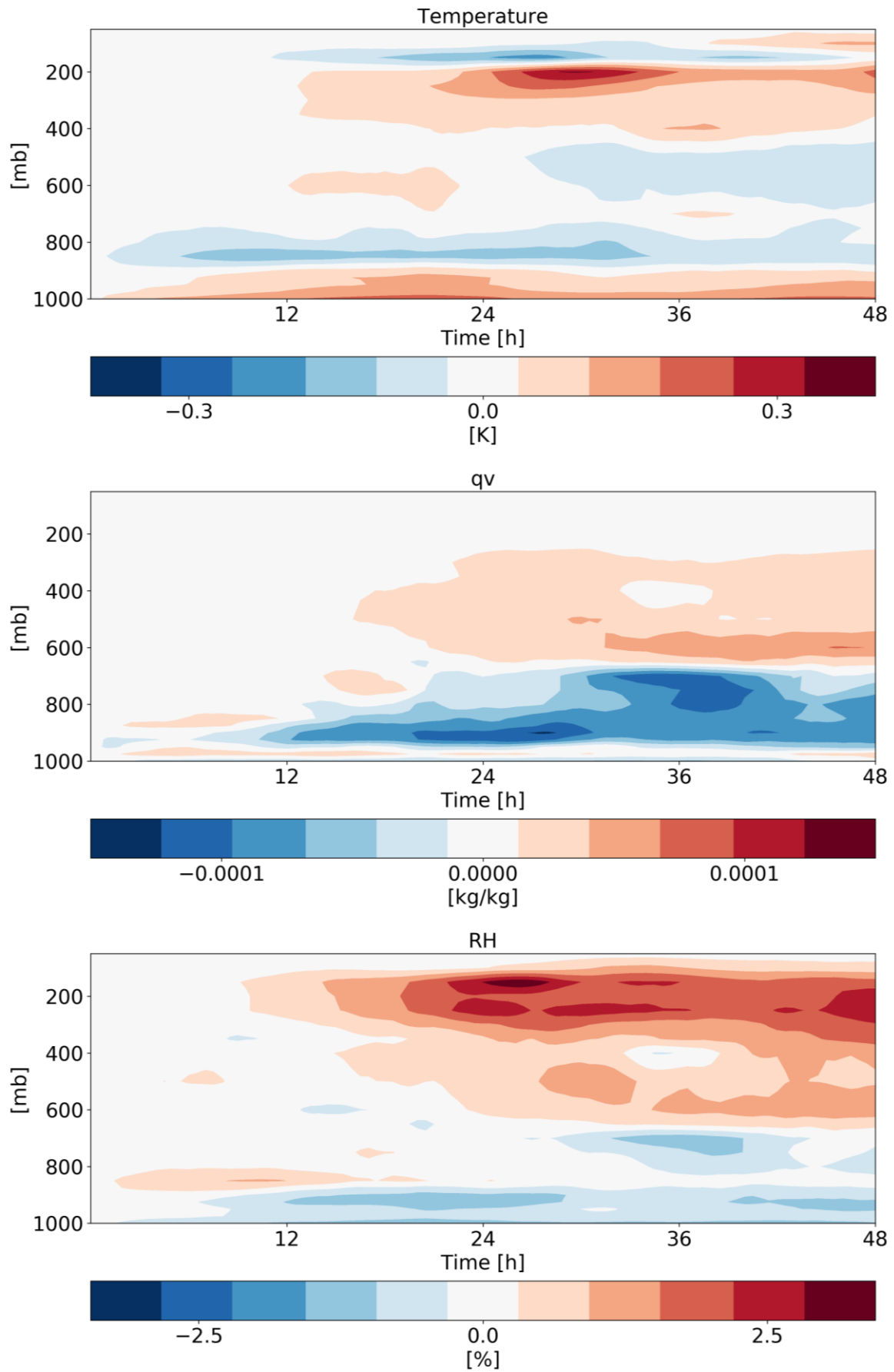
520 property, the mean difference between all combinations of simulations, normalized to a factor 5 increase in
 521 CDNC, and its standard deviation appear in parenthesis.

522



523

524 **Figure 17. Domain and time average vertical profiles for the different CDNC simulations for the shallow-**
 525 **cloud dominated case. The properties that are presented here are: cloud droplet mass mixing ratio (qc – for**
 526 **clouds’ droplets with radius smaller than 40 μm), ice mass mixing ratio (qi), rain mass mixing ratio (qr - for**
 527 **clouds’ drops with radius larger than 40 μm), total water mass mixing ratio ($qt = qc+qi+qr$), and cloud**
 528 **fraction (CF).**

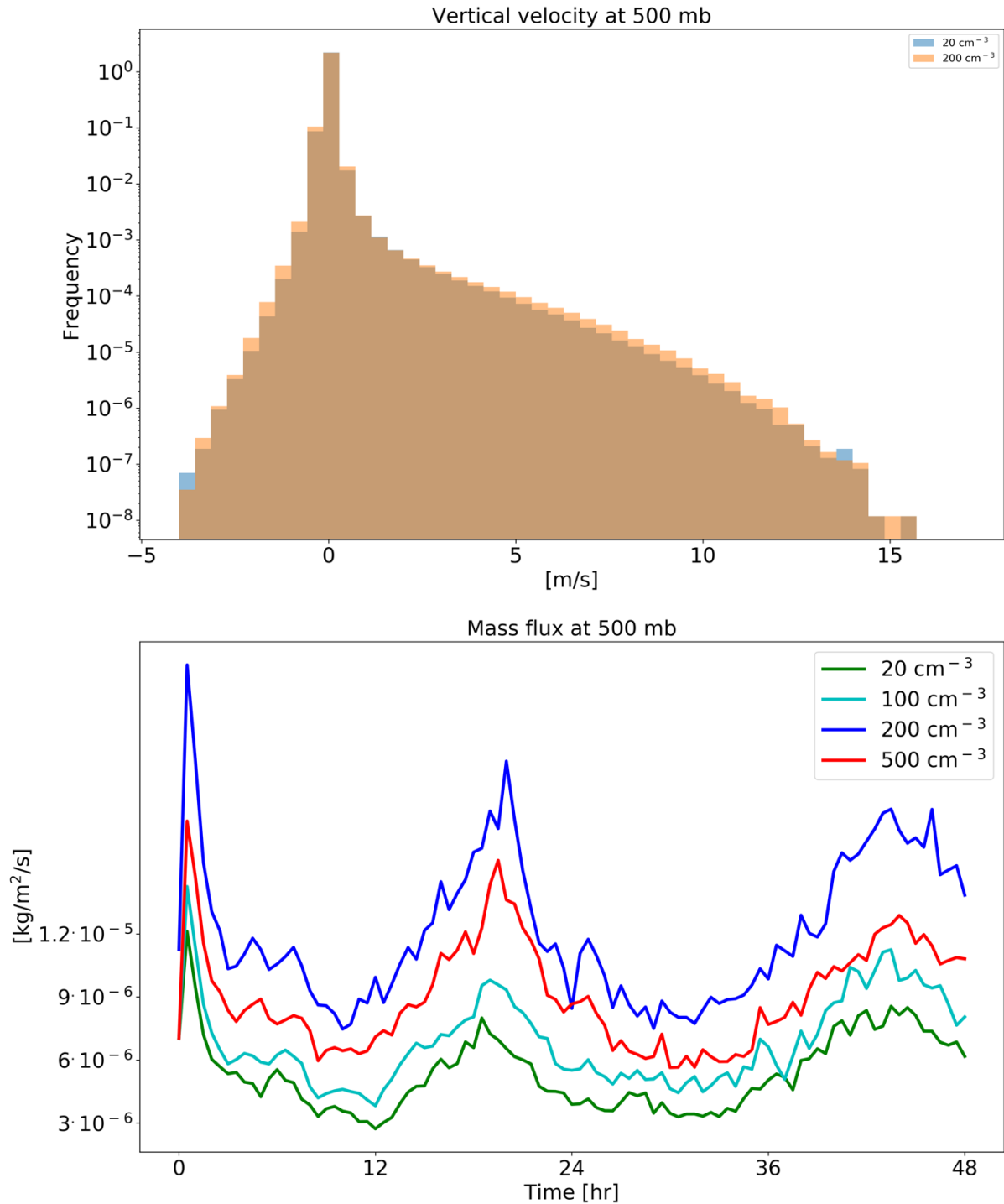


529

530 **Figure 18. Time-height diagrams of the differences in the domain mean temperature, specific humidity (qv)**

531 and relative humidity (RH) vertical profiles between polluted (CDNC = 200 cm⁻³) and clean (CDNC = 20 cm⁻³)
532 ³) simulations for the deep-cloud dominated case (16-18/08/2016).

533



534

535 **Figure 19.** histograms of ICON simulated vertical velocity at the level of 500 mb for a clean (CDNC = 20 cm⁻³) and polluted (CDNC = 200 cm⁻³) simulations (upper), and the time evolution of the net upwards water
536 (liquid and ice) mass flux (lower) for the different CDNC simulations for the deep-cloud dominated case (16-
537

538 **18/08/2016). The 500 mb level is chosen as it represents the transition between the warm part to the cold part**
539 **of the clouds. In the histogram only two simulations are presented for clarity.**

540

541 **Summary and conclusions**

542 Two different case studies of tropical cloud systems over the Atlantic Ocean were simulated
543 using the ICON numerical model in a cloud resolving configuration with 1.2 km resolution and
544 a relatively large domain ($\sim 22^\circ \times 11^\circ$). The cases represent dates from the NARVAL 2 field
545 campaign that took place during August 2016 and have different dominant cloud types and
546 different dominating terms in their energy budget. The first case (10-12/8/2016) is shallow-cloud
547 dominated and hence dominated by radiative cooling, while the second case (16-18/8/2016) is
548 dominated by deep convective clouds and hence dominated by precipitation warming. The main
549 objective of this study is to analyse the response of the atmospheric energy budget to changes in
550 cloud droplet number concentration (CDNC), which serve as a proxy for (or idealized
551 representation of) changes in aerosol concentration. This enables better understanding of the
552 processes acting in global-scale studies trying to constrain aerosol effect on precipitation changes
553 using the energy budget perspective (O’Gorman et al., 2012; Muller and O’Gorman, 2011;
554 Hodnebrog et al., 2016; Samset et al., 2016; Myhre et al., 2017; Liu et al., 2018; Richardson et
555 al., 2018; Dagan et al., 2019a). Our results demonstrate that regional atmospheric energy budgets
556 can be significantly perturbed by changes in CDNC and that the magnitude of the effect is cloud
557 regime dependent (even for a given geographical region and given time of the year as the two
558 cases are separated by less than a week).

559 Figure 20 summarizes the energy and radiation response of the two simulated cases to CDNC
560 perturbations. It shows that the atmosphere in the deep-cloud dominated case experiences a very
561 strong atmospheric warming due to an increase in CDNC (10.0 W/m^2). Most of this warming is
562 caused by a reduction in the outgoing LW radiation at the TOA. The SW radiative fluxes (both
563 at the TOA and surface) is also significantly modified but their net effect on the atmospheric
564 column energy budget is small. The net TOA radiative fluxes change in this case is -1.9 W/m^2 .
565 Beside the atmospheric radiative warming, changes in precipitation ($\sim -0.3 \text{ W/m}^2$), and in sensible
566 heat flux (Q_{SH} , -1.4 W/m^2) also contribute to the total trend as a response of increase in CDNC.
567 We note that since 1 mm/hr of rain is equivalent to 628 W/m^2 , even negligible changes in
568 precipitation of less than 0.5 mm over 48 hr (as seen in our simulations) can still appear as
569 significant changes in the atmospheric energy budget and contribute a few W/m^2 .

570 The response of the radiative fluxes can be explained by the changes in the mean cloud and
571 thermodynamic properties in the domain. The mean cloud fraction (CF) increases with the
572 increase in CDNC (Fig. 16) while the vertical structure of it indicates a reduction in the low
573 cloud fraction (below 800 mb) and an increase in the mid and upper troposphere CF (Fig. 17).
574 The water content (both liquid and ice) also increase with the increase in CDNC (Figs. 16 and
575 17) with increasing amount with height. These changes in the mean cloud properties drive both
576 the reduction in SW fluxes at TOA and surface and LW flux at TOA as the clouds become more
577 opaque (Koren et al., 2010; Storelvmo et al., 2011) and cover a larger fraction of the sky. In
578 addition to cloud responses, the domain-mean thermodynamic conditions change as well (Fig.
579 18). Specifically, the humidity content at the mid and upper troposphere increases with higher
580 CDNC, (due to increase mass flux to the upper troposphere) which further decreases the outgoing
581 LW flux at the TOA. However, the vast majority of the LW effect emerges from the changes in
582 clouds.

583 Both the increase in water vapor and ice content in the upper troposphere are driven by an
584 increase in water mass flux with increasing CDNC to these levels (Fig. 19, (Koren et al., 2005;
585 Rosenfeld et al., 2008; Altaratz et al., 2014; Chen et al., 2017)), which is caused mostly by the
586 increase in the water mixing ratio in the mid-troposphere rather than by increase in vertical
587 velocity (Fig. 19) or in cloud fraction (Fig. 17). The ice content in the upper troposphere is also
588 increased due to reduction in the ice falling speed (Grabowski and Morrison, 2016), while the
589 increased relative humidity at these levels, further increases the ice particle lifetime due to slower
590 evaporation. However, the increase in water mass flux to the upper layers is not accompanied
591 with an increase in precipitation as predicted by the classical “invigoration” paradigm (Altaratz
592 et al., 2014; Rosenfeld et al., 2008), which suggest that some compensating mechanisms are
593 operating (Stevens and Feingold, 2009).

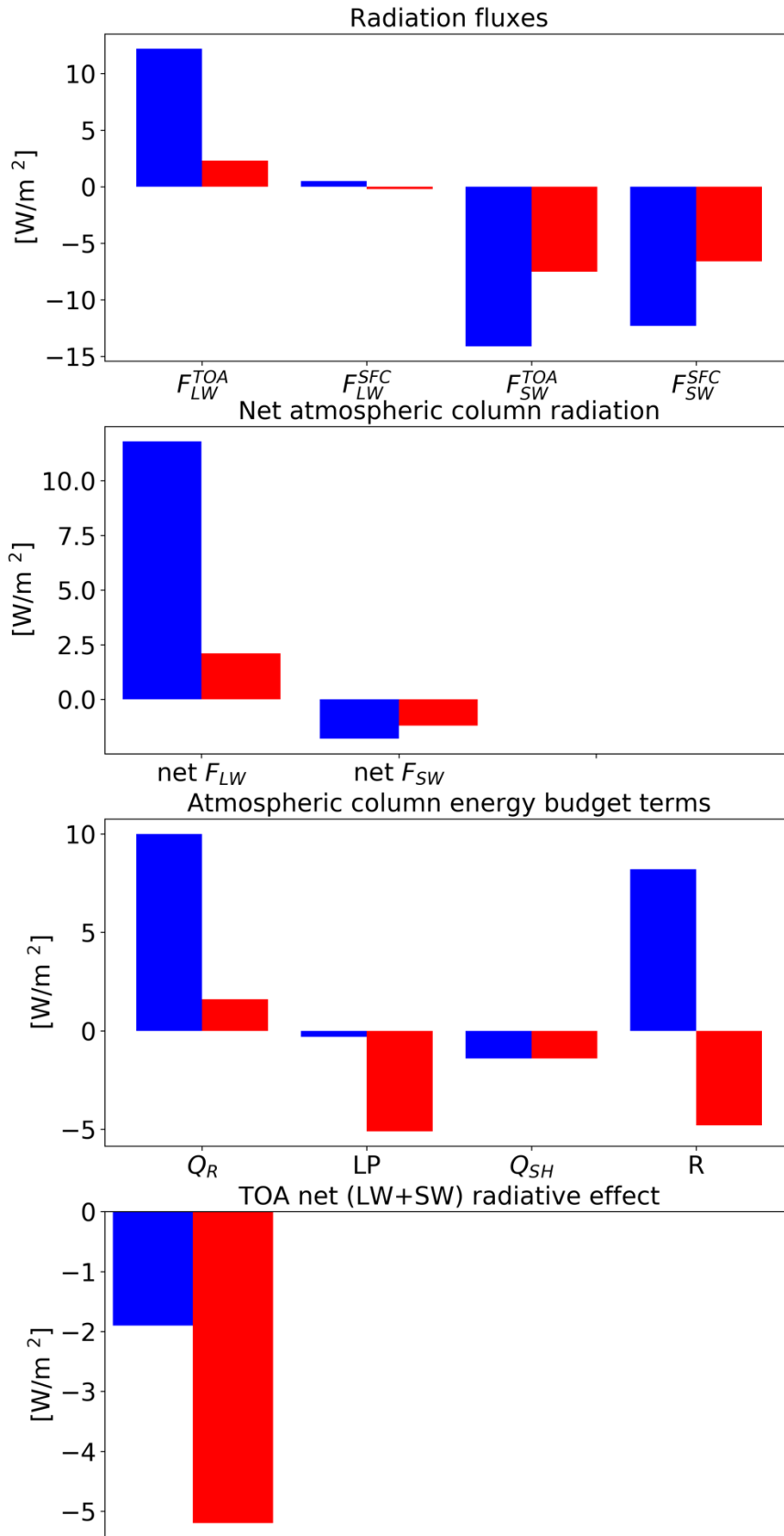
594 In the shallow-cloud dominated case (which also contains a significant amount of deep
595 convection), the response of Q_R is weaker but still substantial (a total decrease in the atmospheric
596 radiative cooling of 1.6 W/m^2 - Fig. 20). The weaker total response under the shallow-cloud
597 dominated conditions is due to the smaller role of the ice part in this case. Here again, the changes
598 in Q_{SH} decrease about -1.4 W/m^2 of this atmospheric warming. As in the deep-cloud dominated
599 case, most of the atmospheric radiative warming is caused by reduction in the outgoing LW flux,
600 while the surface and TOA SW fluxes changes are non-negligible but cancel each other out (in
601 terms of the atmospheric energy budget – reflecting small SW atmospheric absorption changes).
602 However, a significant TOA net (SW+LW) radiative flux change of $\sim -5.2 \text{ W/m}^2$ remains. In this

603 case, the cloud-mean effect on radiation is more complicated. While CF decreases with
604 increasing CDNC, the mean water path (both LWP and IWP) increases (Fig. 8). As in the deep-
605 cloud dominated case, the increase in the water content occurs mostly at the mid and upper
606 troposphere, while the decrease in CF occurs mostly in the lower troposphere (Fig. 9). In terms
607 of the SW fluxes, the effect of the decrease in low CF (decrease SW reflections) and the increase
608 in water mass (increase SW reflections) would partially compensate, while the Twomey effect
609 (Twomey, 1977) adds to the increase SW reflections. In this case, the net effect is more SW
610 reflected back to space at TOA and a net negative flux change (including also the LW).

611 There exists a large spread in estimates of aerosol effects on clouds for different cloud types and
612 different environmental conditions. In this study, as we use a relatively large domain ($22^\circ \times 11^\circ$)
613 and two different dates (each for two days), we sample many different local environmental
614 conditions and cloud types. Such more realistic setups (although with lower spatial resolution)
615 could provide more reliable estimates of aerosol effects on heterogeneous cloud systems than
616 just one-cloud-type, small domain simulations (as was done in many previous studies, e.g (Dagan
617 et al., 2017; Seifert et al., 2015; Ovchinnikov et al., 2014)). However, the conclusions
618 demonstrated here are based on two specific cases. In order to examine the validity of our main
619 conclusions over a wider range of initial conditions, we have conducted a large ensemble of
620 simulations starting from realistic initial conditions (although with a smaller domain) in a
621 companion paper (Dagan and Stier, 2019). These simulations demonstrate that the main
622 conclusions presented in this paper are robust and hold also for a wide range of initial conditions
623 representative for this area. In addition, the realistic setup with the continuously changing
624 boundary conditions and systems that pass through the domain, which are used here, prevent
625 conclusions that might be valid only in cyclic double periodic large eddy simulations, as the
626 background meteorological conditions change more realistically (Dagan et al., 2018b). Another
627 uncertainty in the assessment of the aerosol response are the large differences between different
628 models and microphysical schemes (White et al., 2017; Fan et al., 2016; Khain et al., 2015;
629 Heikenfeld et al., 2019). In this study, as we use only one model, we do not address this
630 uncertainty. In future work we intend to examine the response in multiple models. In addition,
631 more detailed observational constraints on the models are needed. Furthermore, we do not
632 include the temporal evolution of the aerosol concentration. Feedbacks between the aerosol
633 concentration and clouds processes (such as wet scavenging), as well as the direct effects of
634 aerosol on radiation would add another layer of complexity that should be accounted for in future
635 work.

636 Generally, the global mean aerosol radiative forcing is estimated to be negative (Boucher et al.,
637 2013; Bellouin et al., 2019). However, these global aerosol forcing estimates have so far not
638 included the radiative forcing associated with potential effects of aerosols on deep convection –
639 and these effects are not represented in most current climate models due to limitations in
640 convection parameterisations, with only a few exceptions (Kipling et al., 2017; Labbouz et al.,
641 2018). Here we demonstrate the existence of non-negligible aerosol radiative effects (of -5.2 and
642 -1.9 W/m² for the shallow and deep cloud dominated cases, respectively) in tropical cloud
643 systems, that contained both deep and shallow convective clouds, with significant SW and LW
644 contributions. From the (limited) two cases simulated here, it appears that (in agreement with
645 previous studies) the aerosol effect may be regime dependent and that even within a given cloud
646 regime the effect may vary with the meteorological conditions.

647 Finally, we hypothesise that the aerosol impact shown on the atmospheric energy balance, with
648 increasing divergence of dry static energy from deep convective regions concomitantly with
649 increased convergence in shallow clouds regions, can have effects on the large-scale circulation.
650 This should be investigated in future work.



651

652 **Figure 20. Summary of the radiation and energy response to CDNC perturbation in the two different cases.**

653 **Blue represent the deep-cloud dominated case while red the shallow-cloud dominated case.**

654 **Author contributions.** G. D. carried out the simulations and analyses presented. G.C., D.K. and
655 A.S. assisted with the simulations. M.C. assisted with the radiative transfer calculations and
656 comparison with observations. P. S. and A.S. assisted with the design and interpretation of the
657 analyses. G. D. prepared the manuscript with contributions from all co-authors.

658 **Acknowledgements:**

659 This research was supported by the European Research Council (ERC) project constRaining
660 the EffeCts of Aerosols on Precipitation (RECAP) under the European Union's Horizon 2020
661 research and innovation programme with grant agreement No 724602. The simulations were
662 performed using the ARCHER UK National Supercomputing Service. ECMWF is
663 acknowledged for providing Era-interim data set (<https://apps.ecmwf.int/datasets/>). We
664 acknowledge MPI, DWD and DKRZ for the NARVAL simulations. The data presented in the
665 paper can be find in: <https://zenodo.org/record/3611366#.Xi7rHC-cbUI>
666 DOI:10.5281/zenodo.3611366

667

668 **References**

669 Albrecht, B. A.: Aerosols, cloud microphysics, and fractional cloudiness, *Science* (New York, NY), 245,
670 1227, DOI: 10.1126/science.245.4923.1227, 1989.
671 Albrecht, B. A.: Effects of precipitation on the thermodynamic structure of the trade wind boundary
672 layer, *Journal of Geophysical Research: Atmospheres* (1984–2012), 98, 7327-7337,
673 <https://doi.org/10.1029/93JD00027>, 1993.
674 Altaratz, O., Koren, I., Remer, L., and Hirsch, E.: Review: Cloud invigoration by aerosols—Coupling
675 between microphysics and dynamics, *Atmospheric Research*, 140, 38-60,
676 <https://doi.org/10.1016/j.atmosres.2014.01.009>, 2014.
677 Aminou, D.: MSG's SEVIRI instrument, *ESA Bulletin* (0376-4265), 15-17, 2002.
678 Andreae, M. O., Rosenfeld, D., Artaxo, P., Costa, A. A., Frank, G. P., Longo, K. M., and Silva-Dias, M. A.
679 F.: Smoking rain clouds over the Amazon, *Science*, 303, 1337-1342, 10.1126/science.1092779, 2004.
680 Andreae, M. O.: Correlation between cloud condensation nuclei concentration and aerosol optical
681 thickness in remote and polluted regions, *Atmospheric Chemistry and Physics*, 9.2, 543-556, 2009.
682 Arakawa, A., and Schubert, W. H.: Interaction of a cumulus cloud ensemble with the large-scale
683 environment, Part I, *Journal of the Atmospheric Sciences*, 31, 674-701, 1974.
684 Bellouin, N., Quaas, J., Gryspeerdt, E., Kinne, S., Stier, P., Watson-Parris, D., Boucher, O., Carslaw, K.,
685 Christensen, M., and Daniau, A.-L.: Bounding aerosol radiative forcing of climate change, *Reviews of*
686 *Geophysics*, <http://hdl.handle.net/21.11116/0000-0003-9D8D-E>, 2019.
687 Boucher, O., Randall, D., Artaxo, P., Bretherton, C., Feingold, G., Forster, P., Kerminen, V., Kondo, Y.,
688 Liao, H., and Lohmann, U.: Clouds and aerosols, *Climate Change*, 571-657, 2013.
689 Chen, Q., Koren, I., Altaratz, O., Heiblum, R. H., Dagan, G., and Pinto, L.: How do changes in warm-
690 phase microphysics affect deep convective clouds?, *Atmospheric Chemistry and Physics*, 17, 9585-
691 9598, <https://doi.org/10.5194/acp-17-9585-2017>, 2017.

692 Christensen, M. W., Chen, Y. C., and Stephens, G. L.: Aerosol indirect effect dictated by liquid clouds,
693 *Journal of Geophysical Research: Atmospheres*, 121, <https://doi.org/10.1002/2016JD025245>, 2016.

694 Clough, S., Shephard, M., Mlawer, E., Delamere, J., Iacono, M., Cady-Pereira, K., Boukabara, S., and
695 Brown, P.: Atmospheric radiative transfer modeling: a summary of the AER codes, *Journal of*
696 *Quantitative Spectroscopy and Radiative Transfer*, 91, 233-244,
697 <https://doi.org/10.1016/j.jqsrt.2004.05.058>, 2005.

698 Costantino, L., and Bréon, F.-M.: Aerosol indirect effect on warm clouds over South-East Atlantic,
699 from co-located MODIS and CALIPSO observations, *Atmospheric Chemistry and Physics*, 13, 69-88,
700 2013.

701 Dagan, G., Koren, I., and Altaratz, O.: Aerosol effects on the timing of warm rain processes,
702 *Geophysical Research Letters*, 42, 4590-4598, [10.1002/2015GL063839](https://doi.org/10.1002/2015GL063839), 2015a.

703 Dagan, G., Koren, I., and Altaratz, O.: Competition between core and periphery-based processes in
704 warm convective clouds—from invigoration to suppression, *Atmospheric Chemistry and Physics*, 15,
705 2749-2760, <https://doi.org/10.5194/acp-15-2749-2015>, 2015b.

706 Dagan, G., and Chemke, R.: The effect of subtropical aerosol loading on equatorial precipitation,
707 *Geophysical Research Letters*, 43, <https://doi.org/10.1002/2016GL071206>, 2016.

708 Dagan, G., Koren, I., Altaratz, O., and Heiblum, R. H.: Aerosol effect on the evolution of the
709 thermodynamic properties of warm convective cloud fields, *Scientific Reports*, 6, 38769, DOI:
710 [10.1038/srep38769](https://doi.org/10.1038/srep38769), 2016.

711 Dagan, G., Koren, I., Altaratz, O., and Heiblum, R. H.: Time-dependent, non-monotonic response of
712 warm convective cloud fields to changes in aerosol loading, *Atmos. Chem. Phys.*, 17, 7435-7444,
713 [10.5194/acp-17-7435-2017](https://doi.org/10.5194/acp-17-7435-2017), 2017.

714 Dagan, G., Koren, I., and Altaratz, O.: Quantifying the effect of aerosol on vertical velocity and
715 effective terminal velocity in warm convective clouds, *Atmospheric Chemistry and Physics*, 18, 6761-
716 6769, <https://doi.org/10.5194/acp-18-6761-2018>, 2018a.

717 Dagan, G., Koren, I., Altaratz, O., and Lehahn, Y.: Shallow convective cloud field lifetime as a key
718 factor for evaluating aerosol effects, *iScience*, 10, 192-202,
719 <https://doi.org/10.1016/j.isci.2018.11.032>, 2018b.

720 Dagan, G., Koren, I., Kostinski, A., and Altaratz, O.: Organization and oscillations in simulated shallow
721 convective clouds, *Journal of Advances in Modeling Earth Systems*,
722 <https://doi.org/10.1029/2018MS001416>, 2018c.

723 Dagan, G., Stier, P., and Watson-Parris, D.: Contrasting response of precipitation to aerosol
724 perturbation in the tropics and extra-tropics explained by energy budget considerations, *Geophysical*
725 *Research Letters*, <https://doi.org/10.1029/2019GL083479>, 2019a.

726 Dagan, G., Stier, P., and Watson-Parris, D.: Analysis of the atmospheric water budget for elucidating
727 the spatial scale of precipitation changes under climate change, *Geophysical Research Letters*,
728 <https://doi.org/10.1029/2019GL084173>, 2019b

729 Dagan, G. and Stier, P.: Ensemble daily simulations for elucidating cloud–aerosol interactions under a
730 large spread of realistic environmental conditions, *Atmos. Chem. Phys. Discuss.*,
731 <https://doi.org/10.5194/acp-2019-949>, in review, 2019.

732 Dee, D., Uppala, S., Simmons, A., Berrisford, P., Poli, P., Kobayashi, S., Andrae, U., Balmaseda, M.,
733 Balsamo, G., and Bauer, P.: The ERA-Interim reanalysis: Configuration and performance of the data
734 assimilation system, *Quarterly Journal of the royal meteorological society*, 137, 553-597,
735 <https://doi.org/10.1002/qj.828>, 2011.

736 Dey, S., Di Girolamo, L., Zhao, G., Jones, A. L., and McFarquhar, G. M.: Satellite-observed
737 relationships between aerosol and trade-wind cumulus cloud properties over the Indian Ocean,
738 Geophysical Research Letters, 38, <https://doi.org/10.1029/2010GL045588>, 2011.

739 Emanuel, K. A., Neelin, J. D., and Bretherton, C. S.: On large-scale circulations in convecting
740 atmospheres, Quarterly Journal of the Royal Meteorological Society, 120, 1111-1143, 1994.

741 Fan, J., Zhang, R., Li, G., and Tao, W.-K.: Effects of aerosols and relative humidity on cumulus clouds,
742 Journal of Geophysical Research-Atmospheres, 112, 10.1029/2006jd008136, 2007.

743 Fan, J., Yuan, T., Comstock, J. M., Ghan, S., Khain, A., Leung, L. R., Li, Z., Martins, V. J., and
744 Ovchinnikov, M.: Dominant role by vertical wind shear in regulating aerosol effects on deep
745 convective clouds, Journal of Geophysical Research-Atmospheres, 114, 10.1029/2009jd012352,
746 2009.

747 Fan, J., Comstock, J. M., and Ovchinnikov, M.: The cloud condensation nuclei and ice nuclei effects
748 on tropical anvil characteristics and water vapor of the tropical tropopause layer, Environmental
749 Research Letters, 5, 10.1088/1748-9326/5/4/044005, 2010.

750 Fan, J., Leung, L. R., Rosenfeld, D., Chen, Q., Li, Z., Zhang, J., and Yan, H.: Microphysical effects
751 determine macrophysical response for aerosol impacts on deep convective clouds, Proceedings of
752 the National Academy of Sciences, 110, E4581-E4590, <https://doi.org/10.1073/pnas.1316830110>,
753 2013.

754 Fan, J., Wang, Y., Rosenfeld, D., and Liu, X.: Review of aerosol–cloud interactions: Mechanisms,
755 significance, and challenges, Journal of the Atmospheric Sciences, 73, 4221-4252,
756 <https://doi.org/10.1175/JAS-D-16-0037.1>, 2016.

757 Ghan, S. J., Abdul-Razzak, H., Nenes, A., Ming, Y., Liu, X., Ovchinnikov, M., Shipway, B., Meskhidze,
758 N., Xu, J., and Shi, X.: Droplet nucleation: Physically-based parameterizations and comparative
759 evaluation, Journal of Advances in Modeling Earth Systems, 3,
760 <https://doi.org/10.1029/2011MS000074>, 2011.

761 Glassmeier, F., and Lohmann, U.: Constraining precipitation susceptibility of warm-, ice-, and mixed-
762 phase clouds with microphysical equations, Journal of the Atmospheric Sciences, 73, 5003-5023,
763 <https://doi.org/10.1175/JAS-D-16-0008.1>, 2016.

764 Goren, T., and Rosenfeld, D.: Decomposing aerosol cloud radiative effects into cloud cover, liquid
765 water path and Twomey components in marine stratocumulus, Atmospheric research, 138, 378-393,
766 <https://doi.org/10.1016/j.atmosres.2013.12.008>, 2014.

767 Grabowski, W. W., and Morrison, H.: Untangling microphysical impacts on deep convection applying
768 a novel modeling methodology. Part II: Double-moment microphysics, Journal of the Atmospheric
769 Sciences, 73, 3749-3770, <https://doi.org/10.1175/JAS-D-15-0367.1>, 2016.

770 Gryspeerd, E., and Stier, P.: Regime-based analysis of aerosol-cloud interactions, Geophysical
771 Research Letters, 39, <https://doi.org/10.1029/2012GL053221>, 2012.

772 Gryspeerd, E., Stier, P., White, B., and Kipling, Z.: Wet scavenging limits the detection of aerosol
773 effects on precipitation, Atmospheric Chemistry and Physics, 15, 7557-7570,
774 <https://doi.org/10.5194/acp-15-7557-2015>, 2015.

775 Gryspeerd, E., Sourdeval, O., Quaas, J., Delanoë, J., Krämer, M., and Kühne, P.: Ice crystal number
776 concentration estimates from lidar–radar satellite remote sensing–Part 2: Controls on the ice crystal
777 number concentration, Atmospheric Chemistry and Physics, 18, 14351-14370,
778 <https://doi.org/10.5194/acp-18-14351-2018>, 2018b.

779 Gryspeerd, E., Goren, T., Sourdeval, O., Quaas, J., Mülmenstädt, J., Dipu, S., Unglaub, C., Gettelman,
780 A., and Christensen, M.: Constraining the aerosol influence on cloud liquid water path, *Atmospheric*
781 *Chemistry and Physics*, 19, 5331-5347, <https://doi.org/10.5194/acp-19-5331-2019>, 2019.

782 Heikenfeld, M., White, B., Labbouz, L., and Stier, P.: Aerosol effects on deep convection: the
783 propagation of aerosol perturbations through convective cloud microphysics, *Atmospheric*
784 *Chemistry and Physics*, 19, 2601-2627, <https://doi.org/10.5194/acp-19-2601-2019>, 2019.

785 Henderson, D. S., L'Ecuyer, T., Stephens, G., Partain, P., and Sekiguchi, M.: A Multisensor Perspective
786 on the Radiative Impacts of Clouds and Aerosols, *J. Appl. Meteorol. Clim.*, 52, 853– 871,
787 <https://doi.org/10.1175/JAMC-D-12-025.1>, 2013.

788 Hodnebrog, O., Myhre, G., Forster, P. M., Sillmann, J., and Samset, B. H.: Local biomass burning is a
789 dominant cause of the observed precipitation reduction in southern Africa, *Nat Commun*, 7,
790 10.1038/ncomms11236, 2016.

791 Hoose, C., and Möhler, O.: Heterogeneous ice nucleation on atmospheric aerosols: a review of
792 results from laboratory experiments, *Atmospheric Chemistry and Physics*, 12, 9817–9854. 2012.

793 Iacono, M. J., Delamere, J. S., Mlawer, E. J., Shephard, M. W., Clough, S. A., and Collins, W. D.:
794 Radiative forcing by long-lived greenhouse gases: Calculations with the AER radiative transfer
795 models, *Journal of Geophysical Research: Atmospheres*, 113,
796 <https://doi.org/10.1029/2008JD009944>, 2008.

797 Jakob, C., Singh, M., and Jungandreas, L.: Radiative Convective Equilibrium and Organized
798 Convection: An Observational Perspective, *Journal of Geophysical Research: Atmospheres*, 124,
799 5418-5430, 2019.

800 Jeon, Y.-L., Moon, S., Lee, H., Baik, J.-J., and Lkhamjav, J.: Non-Monotonic Dependencies of Cloud
801 Microphysics and Precipitation on Aerosol Loading in Deep Convective Clouds: A Case Study Using
802 the WRF Model with Bin Microphysics, *Atmosphere*, 9, 434, <https://doi.org/10.3390/atmos9110434>,
803 2018.

804 Jiang, H., Xue, H., Teller, A., Feingold, G., and Levin, Z.: Aerosol effects on the lifetime of shallow
805 cumulus, *Geophysical Research Letters*, 33, 10.1029/2006gl026024, 2006.

806 Jiang, J. H., Su, H., Huang, L., Wang, Y., Massie, S., Zhao, B., Omar, A., and Wang, Z.: Contrasting
807 effects on deep convective clouds by different types of aerosols, *Nature communications*, 9, 3874,
808 2018.

809 Kalina, E. A., Friedrich, K., Morrison, H., and Bryan, G. H.: Aerosol effects on idealized supercell
810 thunderstorms in different environments, *Journal of the Atmospheric Sciences*, 71, 4558-4580,
811 <https://doi.org/10.1175/JAS-D-14-0037.1>, 2014.

812 Kaufman, Y. J., Koren, I., Remer, L. A., Rosenfeld, D., and Rudich, Y.: The effect of smoke, dust, and
813 pollution aerosol on shallow cloud development over the Atlantic Ocean, *Proceedings of the*
814 *National Academy of Sciences of the United States of America*, 102, 11207-11212,
815 10.1073/pnas.0505191102, 2005.

816 Khain, A., Rosenfeld, D., and Pokrovsky, A.: Aerosol impact on the dynamics and microphysics of
817 deep convective clouds, *Quarterly Journal of the Royal Meteorological Society*, 131, 2639-2663,
818 10.1256/qj.04.62, 2005.

819 Khain, A., Beheng, K., Heymsfield, A., Korolev, A., Krichak, S., Levin, Z., Pinsky, M., Phillips, V.,
820 Prabhakaran, T., and Teller, A.: Representation of microphysical processes in cloud-resolving models:
821 spectral (bin) microphysics vs. bulk parameterization, *Reviews of Geophysics*,
822 <https://doi.org/10.1002/2014RG000468>, 2015.

823 Khain, A. P., BenMoshe, N., and Pokrovsky, A.: Factors determining the impact of aerosols on surface
824 precipitation from clouds: An attempt at classification, *Journal of the Atmospheric Sciences*, 65,
825 1721-1748, 10.1175/2007jas2515.1, 2008.

826 Khain, A. P.: Notes on state-of-the-art investigations of aerosol effects on precipitation: a critical
827 review, *Environmental Research Letters*, 4, 015004 (015020 pp.)-015004 (015020 pp.),
828 10.1088/1748-9326/4/1/015004, 2009.

829 Kipling, Z., Stier, P., Labbouz, L., and Wagner, T.: Dynamic subgrid heterogeneity of convective cloud
830 in a global model: description and evaluation of the Convective Cloud Field Model (CCFM) in
831 ECHAM6–HAM2, *Atmospheric Chemistry and Physics*, 17, 327-342, [https://doi.org/10.5194/acp-17-](https://doi.org/10.5194/acp-17-327-2017)
832 [327-2017](https://doi.org/10.5194/acp-17-327-2017), 2017.

833 Klepp, C., Ament, F., Bakan, S., Hirsch, L., and Stevens, B.: The NARVAL Campaign Report, 2014.

834 Klocke, D., Brueck, M., Hohenegger, C., and Stevens, B.: Rediscovery of the doldrums in storm-
835 resolving simulations over the tropical Atlantic, *Nature Geoscience*, 10, 891, 2017.

836 Koren, I., Kaufman, Y. J., Rosenfeld, D., Remer, L. A., and Rudich, Y.: Aerosol invigoration and
837 restructuring of Atlantic convective clouds, *Geophysical Research Letters*, 32,
838 10.1029/2005gl023187, 2005.

839 Koren, I., Remer, L. A., Altaratz, O., Martins, J. V., and Davidi, A.: Aerosol-induced changes of
840 convective cloud anvils produce strong climate warming, *Atmospheric Chemistry and Physics*, 10,
841 5001-5010, 10.5194/acp-10-5001-2010, 2010.

842 Koren, I., Dagan, G., and Altaratz, O.: From aerosol-limited to invigoration of warm convective
843 clouds, *science*, 344, 1143-1146, DOI: 10.1126/science.1252595, 2014.

844 Koren, I., Altaratz, O., and Dagan, G.: Aerosol effect on the mobility of cloud droplets, *Environmental*
845 *Research Letters*, 10, 104011, doi:10.1088/1748-9326/10/10/104011, 2015.

846 Labbouz, L., Kipling, Z., Stier, P., and Protat, A.: How Well Can We Represent the Spectrum of
847 Convective Clouds in a Climate Model? Comparisons between Internal Parameterization Variables
848 and Radar Observations, *Journal of the Atmospheric Sciences*, 75, 1509-1524,
849 <https://doi.org/10.1175/JAS-D-17-0191.1>, 2018.

850 Lebo, Z. J., and Morrison, H.: Dynamical effects of aerosol perturbations on simulated idealized
851 squall lines, *Monthly Weather Review*, 142, 991-1009, 2014.

852 Lee, S.-S., Feingold, G., and Chuang, P. Y.: Effect of aerosol on cloud–environment interactions in
853 trade cumulus, *Journal of the Atmospheric Sciences*, 69, 3607-3632, 2012.

854 Lee, S. S., Donner, L. J., and Phillips, V. T. J.: Sensitivity of aerosol and cloud effects on radiation to
855 cloud types: comparison between deep convective clouds and warm stratiform clouds over one-day
856 period, *Atmospheric Chemistry and Physics*, 9, 2555-2575, 2009.

857 Levin, Z., and Cotton, W. R.: *Aerosol pollution impact on precipitation: A scientific review*, Springer,
858 2009.

859 Liu, H., Guo, J., Koren, I., Altaratz, O., Dagan, G., Wang, Y., Jiang, J. H., Zhai, P., and Yung, Y. L.: Non-
860 Monotonic Aerosol Effect on Precipitation in Convective Clouds over Tropical Oceans, *Scientific*
861 *Reports*, 9, 7809, 2019.

862 Liu, L., Shawki, D., Voulgarakis, A., Kasoar, M., Samset, B., Myhre, G., Forster, P., Hodnebrog, Ø.,
863 Sillmann, J., and Aalbergsjø, S.: A PDRMIP Multimodel Study on the impacts of regional aerosol
864 forcings on global and regional precipitation, *Journal of Climate*, 31, 4429-4447, 2018.

865 Lohmann, U., and Hoose, C.: Sensitivity studies of different aerosol indirect effects in mixed-phase
866 clouds, *Atmospheric Chemistry and Physics*, 9, 8917-8934, 2009.

867 Manabe, S., and Strickler, R. F.: Thermal equilibrium of the atmosphere with a convective
868 adjustment, *Journal of the Atmospheric Sciences*, 21, 361-385, 1964

869 Mlawer, E. J., Taubman, S. J., Brown, P. D., Iacono, M. J., and Clough, S. A.: Radiative transfer for
870 inhomogeneous atmospheres: RRTM, a validated correlated-k model for the longwave, *Journal of*
871 *Geophysical Research: Atmospheres*, 102, 16663-16682, 1997.

872 Muller, C., and O’Gorman, P.: An energetic perspective on the regional response of precipitation to
873 climate change, *Nature Climate Change*, 1, 266, 2011.

874 Mülmenstädt, J., and Feingold, G.: The Radiative Forcing of Aerosol–Cloud Interactions in Liquid
875 Clouds: Wrestling and Embracing Uncertainty, *Current Climate Change Reports*, 4, 23-40,
876 <https://doi.org/10.1007/s40641-018-0089-y>, 2018.

877 Myhre, G., Forster, P., Samset, B., Hodnebrog, Ø., Sillmann, J., Aalbergsjø, S., Andrews, T., Boucher,
878 O., Faluvegi, G., and Fläschner, D.: PDRMIP: a precipitation driver and response model
879 intercomparison project—protocol and preliminary results, *Bulletin of the American Meteorological*
880 *Society*, 98, 1185-1198, 2017.

881 O’Gorman, P. A., Allan, R. P., Byrne, M. P., and Previdi, M.: Energetic Constraints on Precipitation
882 Under Climate Change, *Surveys in Geophysics*, 33, 585-608, [https://doi.org/10.1007/s10712-011-](https://doi.org/10.1007/s10712-011-9159-6)
883 [9159-6](https://doi.org/10.1007/s10712-011-9159-6), 2012.

884 Ovchinnikov, M., Ackerman, A. S., Avramov, A., Cheng, A., Fan, J., Fridlind, A. M., Ghan, S.,
885 Harrington, J., Hoose, C., and Korolev, A.: Intercomparison of large-eddy simulations of Arctic mixed-
886 phase clouds: Importance of ice size distribution assumptions, *Journal of Advances in Modeling Earth*
887 *Systems*, 6, 223-248, <https://doi.org/10.1002/2013MS000282>, 2014.

888 Richardson, T., Forster, P., Andrews, T., Boucher, O., Faluvegi, G., Fläschner, D., Hodnebrog, Ø.,
889 Kasoar, M., Kirkevåg, A., and Lamarque, J.-F.: Drivers of precipitation change: An energetic
890 understanding, *Journal of Climate*, 31, 9641-9657, <https://doi.org/10.1175/JCLI-D-17-0240.1>, 2018.

891 Rosenfeld, D.: Suppression of rain and snow by urban and industrial air pollution, *Science*, 287, 1793-
892 1796, [10.1126/science.287.5459.1793](https://doi.org/10.1126/science.287.5459.1793), 2000.

893 Rosenfeld, D., Lohmann, U., Raga, G. B., O’Dowd, C. D., Kulmala, M., Fuzzi, S., Reissell, A., and
894 Andreae, M. O.: Flood or drought: How do aerosols affect precipitation?, *Science*, 321, 1309-1313,
895 [10.1126/science.1160606](https://doi.org/10.1126/science.1160606), 2008.

896 Rosenfeld, D., Wood, R., Donner, L. J., and Sherwood, S. C.: Aerosol cloud-mediated radiative forcing:
897 highly uncertain and opposite effects from shallow and deep clouds, in: *Climate Science for Serving*
898 *Society*, Springer, 105-149, https://doi.org/10.1007/978-94-007-6692-1_5, 2013.

899 Rosenfeld, D., Zhu, Y., Wang, M., Zheng, Y., Goren, T., and Yu, S.: Aerosol-driven droplet
900 concentrations dominate coverage and water of oceanic low-level clouds, *Science*, 363, eaav0566,
901 [DOI: 10.1126/science.aav0566](https://doi.org/10.1126/science.aav0566), 2019.

902 Rothenberg, D., Avramov, A., and Wang, C.: On the representation of aerosol activation and its
903 influence on model-derived estimates of the aerosol indirect effect, *Atmos. Chem. Phys*, 18, 7961-
904 7983, <https://doi.org/10.5194/acp-18-7961-2018>, 2018.

905 Samset, B., Myhre, G., Forster, P., Hodnebrog, Ø., Andrews, T., Faluvegi, G., Flaeschner, D., Kasoar,
906 M., Kharin, V., and Kirkevåg, A.: Fast and slow precipitation responses to individual climate forcings: A
907 PDRMIP multimodel study, *Geophysical Research Letters*, 43, 2782-2791,
908 <https://doi.org/10.1002/2016GL068064>, 2016.

909 Savane, O. S., Vant-Hull, B., Mahani, S., and Khanbilvardi, R.: Effects of Aerosol on Cloud Liquid
910 Water Path: Statistical Method a Potential Source for Divergence in Past Observation Based
911 Correlative Studies, *Atmosphere*, 6, 273-298, <https://doi.org/10.3390/atmos6030273>, 2015.

912 Seifert, A., and Beheng, K.: A two-moment cloud microphysics parameterization for mixed-phase
913 clouds. Part 2: Maritime vs. continental deep convective storms, *Meteorology and Atmospheric*
914 *Physics*, 92, 67-82, <https://doi.org/10.1007/s00703-005-0113-3>, 2006a.

915 Seifert, A., and Beheng, K. D.: A two-moment cloud microphysics parameterization for mixed-phase
916 clouds. Part 1: Model description, *Meteorology and atmospheric physics*, 92, 45-66,
917 <https://doi.org/10.1007/s00703-005-0112-4>, 2006b.

918 Seifert, A., and Heus, T.: Large-eddy simulation of organized precipitating trade wind cumulus
919 clouds, *Atmos. Chem. Phys*, 13, 5631-5645, doi:10.5194/acpd-13-1855-2013, 2013.

920 Seifert, A., Heus, T., Pincus, R., and Stevens, B.: Large-eddy simulation of the transient and near-
921 equilibrium behavior of precipitating shallow convection, *Journal of Advances in Modeling Earth*
922 *Systems*, <https://doi.org/10.1002/2015MS000489>, 2015.

923 Seigel, R. B.: Shallow Cumulus Mixing and Subcloud Layer Responses to Variations in Aerosol
924 Loading, *Journal of the Atmospheric Sciences*, <https://doi.org/10.1175/JAS-D-13-0352.1>, 2014.

925 Simpson, E., Connolly, P., and McFiggans, G.: An investigation into the performance of four cloud
926 droplet activation parameterisations, *Geoscientific Model Development*, 7, 1535-1542,
927 doi:10.5194/gmd-7-1535-2014, 2014.

928 Small, J. D., Chuang, P. Y., Feingold, G., and Jiang, H.: Can aerosol decrease cloud lifetime?,
929 *Geophysical Research Letters*, 36, <https://doi.org/10.1029/2009GL038888>, 2009.

930 Sourdeval, O., Gryspeerd, E., Krämer, M., Goren, T., Delanoë, J., Afchine, A., Hemmer, F., and Quaas,
931 J.: Ice crystal number concentration estimates from lidar–radar satellite remote sensing—Part 1:
932 Method and evaluation, <https://doi.org/10.5194/acp-18-14327-2018> 2018.

933 Spill, G., Stier, P., Field, P. R., and Dagan, G.: Effects of aerosol in simulations of realistic shallow
934 cumulus cloud fields in a large domain, *Atmospheric Chemistry and Physics*,
935 <https://doi.org/10.5194/acp-2019-432>, 2019.

936 Stephens, G. L., Gabriel, P. M., and Partain, P. T.: Parameterization of atmospheric radiative transfer.
937 Part I: Validity of simple models, *Journal of the atmospheric sciences*, 58, 3391-3409,
938 [https://doi.org/10.1175/1520-0469\(2001\)058%3C3391:POARTP%3E2.0.CO;2](https://doi.org/10.1175/1520-0469(2001)058%3C3391:POARTP%3E2.0.CO;2), 2001.

939 Stevens, B., and Feingold, G.: Untangling aerosol effects on clouds and precipitation in a buffered
940 system, *Nature*, 461, 607-613, 10.1038/nature08281, 2009.

941 Stevens, B., Farrell, D., Hirsch, L., Jansen, F., Nuijens, L., Serikov, I., Brüggemann, B., Forde, M., Linne,
942 H., and Lonitz, K.: The Barbados Cloud Observatory: Anchoring investigations of clouds and
943 circulation on the edge of the ITCZ, *Bulletin of the American Meteorological Society*, 97, 787-801,
944 2016.

945 Stevens, B., Ament, F., Bony, S., Crewell, S., Ewald, F., Gross, S., Hansen, A., Hirsch, L., Jacob, M., and
946 Kölling, T.: A high-altitude long-range aircraft configured as a cloud observatory—the NARVAL
947 expeditions, *Bulletin of the American Meteorological Society*, <https://doi.org/10.1175/BAMS-D-18-0198.1>, 2019.

949 Storelvmo, T., Hoose, C., and Eriksson, P.: Global modeling of mixed-phase clouds: The albedo and
950 lifetime effects of aerosols, *Journal of Geophysical Research: Atmospheres*, 116,
951 <https://doi.org/10.1029/2010JD014724>, 2011.

952 Tao, W.-K., Chen, J.-P., Li, Z., Wang, C., and Zhang, C.: Impact of aerosols on convective clouds and
953 precipitation, *Reviews of Geophysics*, 50, RG2001, <https://doi.org/10.1029/2011RG000369>, 2012.

954 Twomey, S.: The influence of pollution on the shortwave albedo of clouds, *Journal of the*
955 *atmospheric sciences*, 34, 1149-1152, 1977.

956 van den Heever, S. C., Stephens, G. L., and Wood, N. B.: Aerosol Indirect Effects on Tropical
957 Convection Characteristics under Conditions of Radiative-Convective Equilibrium, *Journal of the*
958 *Atmospheric Sciences*, 68, 699-718, [10.1175/2010jas3603.1](https://doi.org/10.1175/2010jas3603.1), 2011.

959 Varble, A.: Erroneous attribution of deep convective invigoration to aerosol concentration, *Journal*
960 *of the Atmospheric Sciences*, 75, 1351-1368, <https://doi.org/10.1175/JAS-D-17-0217.1>, 2018.

961 White, B., Gryspeerd, E., Stier, P., Morrison, H., Thompson, G., and Kipling, Z.: Uncertainty from
962 choice of microphysics scheme in convection-permitting models significantly exceeds aerosol effects,
963 *Atmospheric Chemistry and Physics*, 7, <https://doi.org/10.5194/acp-17-12145-2017>, 2017.

964 Williams, E., Rosenfeld, D., Madden, N., Gerlach, J., Gears, N., Atkinson, L., Dunnemann, N.,
965 Frostrom, G., Antonio, M., and Biazon, B.: Contrasting convective regimes over the Amazon:
966 Implications for cloud electrification, *J. Geophys. Res.*, 107, <https://doi.org/10.1029/2001JD000380>,
967 2002.

968 Xue, H., and Feingold, G.: Large-eddy simulations of trade wind cumuli: Investigation of aerosol
969 indirect effects, *Journal of the atmospheric sciences*, 63, 1605-1622,
970 <https://doi.org/10.1175/JAS3706.1>, 2006.

971 Yuan, T., Remer, L. A., Pickering, K. E., and Yu, H.: Observational evidence of aerosol enhancement of
972 lightning activity and convective invigoration, *Geophysical Research Letters*, 38,
973 [10.1029/2010gl046052](https://doi.org/10.1029/2010gl046052), 2011a.

974 Yuan, T., Remer, L. A., and Yu, H.: Microphysical, macrophysical and radiative signatures of volcanic
975 aerosols in trade wind cumulus observed by the A-Train, *Atmospheric Chemistry and Physics*, 11,
976 7119-7132, [10.5194/acp-11-7119-2011](https://doi.org/10.5194/acp-11-7119-2011), 2011b.

977 Zängl, G., Reinert, D., Rípodas, P., and Baldauf, M.: The ICON (ICOsahedral Non-hydrostatic)
978 modelling framework of DWD and MPI-M: Description of the non-hydrostatic dynamical core,
979 *Quarterly Journal of the Royal Meteorological Society*, 141, 563-579,
980 <https://doi.org/10.1002/qj.2378>, 2015.

981